



1 A Study of the Longer Term Variation of Aerosol Optical Thickness and Direct
2 Shortwave Aerosol Radiative Effect Trends Using MODIS and CERES

3

4

5 Ricardo Alfaro-Contreras¹, Jianglong Zhang¹, Jeffrey S. Reid², and Sundar Christopher³

6 ¹Department of Atmospheric Sciences, University of North Dakota, Grand Forks, ND

7 ²Marine Meteorology Division, Naval Research Laboratory, Monterey, CA

8 ³Department of Atmospheric Science, The University of Alabama in Huntsville

9

10

11

12

13

14

15

16 Corresponding Author: jzhang@atmos.und.edu

17



18 **Abstract**

19 By combining Collection 6 Moderate Resolution and Imaging Spectroradiometer (MODIS)
20 and Version 22 Multi-angle Imaging Spectroradiometer (MISR) aerosol products with Cloud and
21 Earth's Radiant Energy System (CERES) flux products, the aerosol optical thickness (AOT, at
22 $0.55\mu\text{m}$) and Short-Wave Aerosol Radiative Effect (SWARE) trends are studied over ocean for
23 the near full Terra (2000-2015) and Aqua (2002-2015) data records. Despite differences in
24 sampling methods, regional SWARE and AOT trends are highly correlated with one another. Over
25 global oceans, weak SWARE (cloud free SW flux) and AOT trends of $0.5 - 0.6 \text{ Wm}^{-2}$ (-0.5 to -0.6
26 Wm^{-2}) and $0.002 \text{ AOT decade}^{-1}$ were found using Terra data. Near zero AOT and SWARE trends
27 are also found for using Aqua data, regardless of Angular Distribution Models (ADMs) used.
28 Regionally, positive SWARE and AOT trends are found over the Bay of Bengal, Arabian Sea,
29 Arabian/Persian Gulf and the Red Sea, while statistically significant negative trends are derived
30 over the Mediterranean Sea and the eastern US coast. In addition, the global mean instantaneous
31 SW aerosol direct forcing efficiencies are found to be $\sim -60 \text{ Wm}^{-2}$ per AOT, with corresponding
32 SWARE values of $\sim -7 \text{ Wm}^{-2}$ from both Aqua and Terra data, and again, regardless of CERES
33 ADMs used. Regionally, SW aerosol direct forcing efficiency values of $\sim -40 \text{ Wm}^{-2}$ per AOT are
34 found over the southwest coast of Africa where smoke aerosol particles dominate in summer.
35 Larger (in magnitude) SW aerosol direct forcing efficiency values of -50 to -80 Wm^{-2} per AOT
36 are found over several other dust and pollutant aerosol dominated regions. Lastly, the AOT and
37 SWARE trends from this study are also inter-compared with aerosol trends (such as active-based)
38 from several previous studies. Findings suggest that a cohesive understanding of the changing
39 aerosol skies can be achieved through the analysis of observations from both passive- and active-
40 based analyses, as well as at both narrow-band and broad-band data sets.



41 **1. Introduction**

42 The significance of aerosol particles on global and regional climate variations has been
43 extensively studied for the past two decades with both observational- and modeling-based
44 approaches (IPCC, 2013). In particular, studies have suggested that the direct shortwave (SW)
45 Aerosol Radiative Effect (SWARE), which refers to the impacts of aerosol particles on Earth's
46 radiation balance through the absorption and scattering of incoming SW solar energy, can be
47 estimated with the combined use of broadband and narrowband observations at the shortwave
48 spectrum (e.g. Zhang et al., 2005a;b; Loeb and Kato, 2002). For example, using one year of
49 collocated Terra Moderate Resolution Imaging Spectroradiometer (MODIS) and Cloud and
50 Earth's Radiant Energy System (CERES) data, Zhang et al., (2005b) derived the spatial
51 distribution of SWARE over global oceans. In that study, the perturbations in Top-of-Atmosphere
52 (TOA) SW energy due to aerosol particles are estimated using Terra CERES observations. The
53 Terra CERES observations have a large footprint of ~20 km at nadir (Wielicki et al., 1996). Thus,
54 collocated finer resolution Terra MODIS observations are used for cloud-clearing and detecting
55 aerosol plumes within the CERES field of views (Christopher and Zhang, 2002b; Zhang et al.,
56 2005a;b).

57 Terra MODIS, CERES, and Multi-Angle Imaging Spectroradiometer (MISR; Kahn et al.,
58 2010) instruments have been continuously observing Earth's atmosphere for more than 16 years
59 (2000-2016). Similarly, the MODIS and CERES instruments on board the Aqua satellite have
60 also been in operation for 14 years (2002-2016). These datasets derived from sensors onboard the
61 Terra and Aqua satellites are long enough to enable climatological analyses of the longer-term
62 variations in both aerosol concentrations and aerosol induced SW direct climate forcing. Taking
63 advantage of these longer term datasets from the Aqua and Terra satellites, several studies have
64 already examined temporal variations in AOT both on regional and global scales (e.g., Zhang and



65 Reid, 2010, Hsu et al., 2012; Li et al., 2014; Alfaro-Contreras, 2016, Toth et al., 2016). For
66 example, using 10 years (2000-2009) of Collection 5 (C5) Terra and Aqua MODIS Dark Target
67 (DT) AOT data, Zhang and Reid, (2010) found a negligible AOT trend over global oceans, but
68 documented three regions with statistically significant increases in aerosol loadings, including the
69 Indian Bay of Bengal, the Arabian Sea, and the eastern coast of China. Several other studies have
70 also investigated AOT trends using ground-based Aerosol Robotic NETwork (AERONET) data
71 (Li et al., 2014), space borne lidar observations (Toth et al., 2016) and other passive-based
72 observations such as Sea-Viewing Wide Field-of-View Sensor (SeaWiFS, Hsu et al., 2012).

73 Still, to our knowledge, SWARE trends have not been studied with the use of both Terra and
74 Aqua data sets. In addition, the new Collection 6 (C6) MODIS aerosol products have changed the
75 magnitudes of global AOT fields significantly (Levy et al., 2013). Thus, in this study, using C6
76 MODIS and MISR aerosol products, as well as CERES data, we studied AOT and SWARE trends
77 over global oceans with a goal of exploring the following scientific questions:

- 78 1) To what extent have trends changed with the update from MODIS C5 to C6?
- 79 2) What are the regional and global AOT trends over global oceans with the use of near the
80 full Terra/Aqua MODIS and Terra MISR data records?
- 81 3) What are the regional and global trends in MODIS and CERES-based SWARE (Note that
82 although MODIS data are used for cloud clearing, CERES inferred SWAREs are independent of
83 forward calculations of MODIS and MISR)?
- 84 4) What are the instantaneous SW aerosol direct forcing efficiencies and SWARE values on
85 both regional and global scales using near the full Aqua and Terra data records?
- 86 5) Can cohesive conclusions (trend patterns) be achieved among passive-, active-based AOT
87 as well as SWARE trend analyses?



88 This paper is organized as follows. Data used in this study are described in Section 2. In
89 Section 3, differences in AOT trends using C5 and C6 MODIS DT aerosol products are examined
90 for the study period of 2000-2009, and then AOT trends are further derived with the use of near
91 full Terra MODIS and MISR (2000-2015) as well as Aqua MODIS (2002-2015) data records. In
92 Section 4, regional and global SW aerosol direct forcing efficiencies, magnitudes of SWAREs, as
93 well as trends in SWARE are studied using collocated CERES and C6 MODIS DT aerosol
94 products over global oceans. An uncertainty analysis in the derived SWARE trends is also carried
95 in section 4. In Section 5, regional-based AOT and SWARE trends derived from this study are
96 inter-compared with aerosol trend analyses estimated from several other studies that use the
97 CALIOP, MODIS and MISR instruments. Conclusions and discussions are provided in Section
98 6.

99

100 2. Datasets

101 Eight satellite data sets are included in this study (also shown in Table 1). Regional and global
102 over ocean AOTs were extracted from C6 Terra (MOD04_L2, 2000-2015), Aqua (MYD04_L2,
103 2002-2015) MODIS DT level-2 aerosol products (Levy et al., 2013) and Version 22 MISR (2000-
104 2015) aerosol products. The Edition 3 Terra and Aqua CERES ERBElke (ES-8; Barkstrom and
105 Wielicki, 1996) and CERES Single Satellite Footprint (SSF; Loeb and Kato, 2002) Level 2 swath
106 products provide instantaneous broadband SW fluxes. CALIOP Level 2 5-km cloud layer products
107 (Winker et al., 2010) are also used to assist the cirrus cloud-related analysis.

108 *2.1 MODIS DT aerosol products:* The over ocean C6 MODIS DT aerosol products include
109 spectral AOT retrievals at seven wavelengths ranging from visible to Shortwave Infrared at a 10
110 km nadir spatial resolution, with an increased resolution of 20x48 km near the edge of the swath



111 (Levy et al., 2013). Only the 550 nm AOT products are used in this study. Compared to the over
112 ocean C5 MODIS DT products, aside from changes in upstream products such as L1B reflectance,
113 geolocation, land/sea and cloud mask, one major change included in the over ocean C6 MODIS
114 DT data is the use of non-static near surface wind speeds in the retrieval process (Levy et al.,
115 2013). In this study, only AOT retrievals with a Quality Assurance (QA) flag of marginal
116 confidence or higher are used. The reported uncertainty in AOT data is on the order of $(-0.02 \cdot \text{AOT}$
117 $- 10\%)$, $(+0.04 \cdot \text{AOT} + 10\%)$ (e.g. Levy et al., 2013), although several studies suggest that higher
118 uncertainties could be found for individual retrievals (e.g., Shi et al., 2011).

119 *2.2 MISR aerosol products:* On board the Terra satellite platform, the MISR instrument
120 provides observations at nine different viewing zenith angles ($\text{VZA} = 0$ (nadir), $\pm 26.1^\circ$, $\pm 45.6^\circ$,
121 $\pm 60.0^\circ$, $\pm 70.5^\circ$) at four different spectral bands ranging from 446 to 866 nm, although like MODIS
122 we focus on the green wavelength here (558 nm). Even though MISR has a much narrower swath
123 of ~ 360 km in comparison to MODIS (Diner et al., 2002), the multi-angle observations from MISR
124 enable a more reliable AOT retrieval over bright scenes such as desert regions (Kahn et al., 2010).
125 Thus, unlike the MODIS and CERES-based analyses in this study, which focus on global oceans,
126 trend analyses from MISR include both land and ocean regions, unless otherwise stated.

127 *2.3 CERES SSF products and issues:* The CERES SSF data are constructed through weighted
128 averaging of MODIS aerosol and cloud retrievals within a CERES footprint based on CERES
129 point spread function (PSF, Loeb et al., 2003; Geier et al., 2003). The CERES instrument measures
130 TOA broadband radiance, to convert from radiance to flux, angular distribution models (ADMs)
131 are needed (e.g. Loeb et al., 2003). For the CERES SSF products, CERES ADMs (Loeb et al.,
132 2003) are used to convert CERES radiance to flux. Over cloud free oceans, AOT is accounted for
133 in CERES ADMs through the use of the radiative transfer modeled anisotropic factors, stratified



134 as sea salt AOT values (Loeb et al., 2003), without considering the impacts of absorbing aerosols.
135 The CERES SSF data cannot be directly used in this study, however, simply because it is
136 constructed with the MODIS products in active production at the time of data collection. That is,
137 both Collection 4 (C4; before April 2006) and C5 (after April 2006) MODIS DT aerosol data were
138 used in constructing CERES SSF data ([http://ceres.larc.nasa.gov/products.php?product=SSF-](http://ceres.larc.nasa.gov/products.php?product=SSF-Level2)
139 [Level2](http://ceres.larc.nasa.gov/products.php?product=SSF-Level2)). This creates a problem for using CERES SSF in trend analysis, as changes are expected
140 in both global and regional estimations of AOTs between C4 and C5 MODIS DT aerosol products.
141 In addition, C6 MODIS aerosol data, which are currently available, are not included in the CERES
142 SSF data for the study period. Thus, the CERES SSF data are used in this study by collocating
143 with CERES ES-8 and C6 MODIS DT data, which are explained in detail later.

144 *2.4 CERES ES-8 products:* The CERES ES-8 data are also available for the near full Terra
145 and Aqua data records. The CERES ES-8 data are constructed by using ADMs from the Earth
146 Radiation Budget Experiment (ERBE)-like algorithm (Suttles et al., 1988). No aerosol properties
147 are considered in constructing ERBE ADMs and aerosols are usually classified either as clear or
148 partly cloudy pixels. Thus, CERES ES-8 data are used for evaluating the impact of ADMs on
149 CERES derived SWAREs, and for inter-comparison with CERES SSF-based analyses in this
150 study.

151 *2.5 Collocated CERES SSF, ES-8 and MODIS DT products:* CERES SSF, CERES ES-8 and
152 C6 MODIS DT datasets were collocated in this study using 14 years of Aqua and 16 years of Terra
153 data. This is achieved by collocating CERES SSF and ES-8 data as the first step. Note that CERES
154 SSF data include geolocations at surface yet CERES ES-8 data report geolocations at TOA, thus,
155 the collocation is performed by selecting pairs of pixel-level data points from both products that
156 are in the vicinity of each other (less than 2 degree Latitude/Longitude) and have identical raw



157 observations (CERES upward “TOT filtered radiance” and “SW filtered radiance”). Also, CERES
158 SSF reported “Clear area percent coverage at subpixel resolution” values, which are used to define
159 the clear area percentage (CP) in this study, are applied as the initial cloud screen method. Only
160 collocated CERES SSF / ES-8 pairs that have CP values of 95% or higher are included in further
161 analyses.

162 As the second step, the collocated CERES SSF and ES-8 data are further collocated with C6
163 MODIS DT data. Only MODIS and CERES data that are from the same satellite platform are used
164 in the collocation. To collocate MODIS and CERES data, surface geolocations
165 (Latitudes/Longitudes) of both datasets are first identified and the two datasets are collocated in
166 space and time based on the PSF of the CERES instrument (Wielicki et al. 1996, Christopher and
167 Zhang, 2002a;b, Zhang and Christopher, 2003). Also, since MODIS DT products have a spatial
168 resolution of 10-km at nadir, only arithmetic averages are performed for MODIS data points that
169 are within a CERES footprint.

170 CERES data are available from three scan modes: the cross-track, rotating azimuth plane scan,
171 and fixed azimuth plane scan modes. To maintain data consistency, only cross track mode CERES
172 data from Terra and Aqua are used in this study. Also, to further screen potential noisy data, only
173 CERES observations with valid SW flux retrievals (from CERES-ES-8 or CERES SSF) and
174 viewing zenith angle (VZA) as well as solar zenith angle (SZA) less than 60 degrees are considered
175 in this study. Overland observations are further excluded in the study by only using collocated
176 pairs that have CERES ES-8 scene ID of “Clear Ocean”, “Partly Cloudy Over Ocean” and “Mostly
177 Cloudy Over Ocean”. Cloud and aerosol properties within a CERES observation are reported
178 based on the collocated C6 MODIS DT products. The following ancillary data are also recorded
179 for each CERES observation: total number of collocated C6 MODIS DT retrievals, number of



180 valid C6 MODIS DT retrievals (with valid cloud fraction and AOT values), number of valid C6
181 MODIS DT retrievals with QA flags of “marginal”, “good” and “very good”. Lastly, only CERES
182 pixels with CP larger than 99% and a reported MODIS cloud fraction (CF) of less than 1% and are
183 used in this study and the impacts of cloud contamination on the derived SWARE trends are also
184 evaluated later in this paper.

185 *2.6 Collocate CERES ES-8, MODIS DT and CALIOP products:* Using collocated CALIOP
186 and MODIS observations, Toth et al. (2013) suggests that even MODIS detected cloud free scenes
187 may be contaminated with optically thin cirrus clouds (OTC). To further study the effects of OTC
188 on the trend analysis, the 5 km CALIOP cloud layer product (Winker et al., 2010) is utilized. The
189 CALIOP cloud layer (CAL_LID_L2_05kmCLay) data are spatiotemporally collocated with the
190 already collocated MODIS-CERES data sets on-board the Aqua platform. CALIPSO’s Feature
191 Classification Flag is used to locate residual OTC within CERES observations. It should be noted
192 that CALIOP’s data record spans only about half of our study period (June 2006 – Dec. 2015) and
193 is available only on the Aqua platform, thus it will be used as a secondary analysis presented in
194 Section 4.2. Note the CERES CALIPSO CloudSat MODIS (C3M) products, which are
195 constructed by collocating CERES SSF, CALIPSO, CloudSat and MODIS data (Kato et al., 2011),
196 are also available from 2006-2011 (<https://ceres.larc.nasa.gov/products.php?product=CCCM>).
197 However, the C3M data are not available after 2011. Also, to avoid decoupling the impacts of
198 ADMs and cirrus cloud effects, a simple approach, as mentioned in this section is used in this
199 study.

200 *2.7 Estimating trend significance:* Lastly, trend significances are computed based on two
201 statistical methods. To be consistent with Zhang and Reid (2010), the Weatherhead method
202 (Weatherhead et al., 1998, hereafter WH) is used to calculate trend significances for monthly-



203 based AOT data. To increase data samples, SWARE values are estimated/averaged on a seasonal
204 basis. However, the WH method is applicable to monthly data and thus, the Mann-Kendall method
205 (e.g. Mann, 1945; Kendall, 1975) is used to estimate trend significances for seasonal-based
206 analyses. For comparison purposes, both methods are applied to the AOT trend analysis as
207 mentioned in Sections 3 and 4, wherever applicable.

208

209 **3. AOT trends from over ocean DT MODIS data**

210 To initiate this study, we begin with an update to global trend analyses in AOT. Included are
211 two components. First, we evaluate if recent changes in the MODIS aerosol product affect past
212 conclusions on regional aerosol trends over the globe. This is followed by an extension of the trend
213 analysis to the entire 2000-2015 study period (Section 3.2).

214 **3.1 Update of AOT trends from Collection 5 to Collection 6**

215 In the Zhang and Reid (2010) trend paper, 10 years of C5 DT MODIS over ocean data were
216 used in deriving regional and global AOT trends. With the recent release of C6 Aqua and Terra
217 DT MODIS data, including significant updates to calibration and cloud clearing algorithms, it is
218 worth a short reproduction of this work with current products.

219 Similar to Zhang and Reid (2010), Level 2 C6 DT over water Terra MODIS data were binned
220 into $1^\circ \times 1^\circ$ (Latitude/Longitude) monthly averages. “Bad” retrievals, as indicated by the QA flag
221 included in the dataset, are discarded from the analysis, as were MODIS cloud fraction above 80%
222 to minimize the effect of cloud contamination (Zhang and Reid, 2010). Using the monthly gridded
223 over-ocean C6 Terra MODIS DT data from 2000-2009 (excluding August 2000 and June 2001 as
224 these months contained less than 20 days of valid data), regional AOT trends, as well as trend
225 significances (based on WH, as suggested from Zhang and Reid, 2010) were derived and are shown



226 in Figure 1a. To create Figure 1, data are deseasonalized by removing 10-year averages from any
227 given month, for each grid point. Also, AOT trends are derived only for bins which have more
228 than 72 months (60%) of valid data records. In Figure 1a, regions with statistically significant
229 trends at a 95% confidence interval (from WH), are highlighted with black dots.

230 To inter-compare AOT trend analysis from Zhang and Reid (2010), AOT trends from 10
231 selected regions, including north west coast of Africa (8°N - 24°N, 60°W - 18°W), India Bay of
232 Bengal (10°N - 25°N, 78°E - 103°E), eastern coast of China (20°N - 40°N, 110°E - 125°E), Central
233 America (5°N - 20°N, 120°W - 90°W), Arabian Sea (5°N - 23°N, 50°E - 78°E), Mediterranean
234 Sea (30°N - 45°N, 0° - 40° E), south west coast of Africa (23°S - 7°S, 20°W - 15°E), eastern coast
235 of North America (30°N - 45°N, 80°W - 60° W), south east coast of Africa (27° - 15°S, 32°E -
236 45°E), and southeast Asia (15°S - 10°N, 80°E - 120°E) are computed as shown in Table 2. Also,
237 suggested from Zhang and Reid (2010), the AOT trend from Remote Ocean (RO, 40° S - 0°, 179°
238 W - 140° W) is used as a proxy for unrealized bias in the AOT trend due to issues such as
239 calibration and signal drifts, as this is the region that is least affected by any major aerosol plumes
240 originated from main continents. For illustrative purposes, the ratios and differences in AOT
241 trends for both C6 and C5 Terra MODIS based analysis are also shown in Figs. 1e and 1f,
242 respectively, for the study period of 2000-2009. Only grids with AOT trends above or below
243 ± 0.002 AOT/year are used in this comparison.

244 As suggested from Table 2, both AOT trends and trend significances (based on WH) are similar
245 with the use of C5 and C6 Terra MODIS DT over ocean data for the study period of 2000-2009.
246 This suggests that although documentable changes are made to the C6 MODIS DT over ocean data
247 (Levy et al., 2013), the impact of those changes on global and regional AOT trend analysis is rather
248 marginal. For a comparison purpose, Table 2 also includes trend significances derived using the



249 Mann-Kendall method ($|z|$) for the C6 MODIS DT-based analysis, and consistent results are found
250 from both methods a majority of the time.

251 Lastly, for illustrative purposes, regional and global averages over ocean C5 and C6 Terra
252 MODIS DT AOTs are also shown in Table 2 for the period of 2000-2009. Note that in Zhang and
253 Reid (2010), data-assimilation quality C5 MODIS DT data, which is implemented with extensive
254 QA steps (e.g. Zhang and Reid, 2006; Shi et al., 2011), were used. Here regional and global mean
255 C5 AOTs are derived using similar steps as were used in constructing the C6 AOT data. Also, as
256 suggested from Zhang and Reid (2010), although QA steps could lower the mean global over ocean
257 AOTs from ~ 0.15 to ~ 0.11 , in part due to the removal of cloud contaminated retrievals, minor
258 impacts on the AOT trend analysis are reported. As suggested from Table 2, a 10% reduction in
259 global mean over ocean AOT is found for the C6 MODIS DT data in comparing with the C5 data,
260 possibly due to a reduction in marine background AOTs (e.g., the Enhanced Southern Ocean
261 Anomaly feature, as shown in Toth et al., 2013, no longer exists in the C6 product).

262

263 **3.2 AOT trends from near full Terra and Aqua data records**

264 Extending the analysis from the previous section, AOT trends are evaluated for the near full
265 available data record (March 2000 – December 2015 for MODIS Terra and MISR, and July 2002
266 – December 2015 for MODIS Aqua) of C6 over ocean MODIS DT and MISR aerosol products.
267 The C6 MODIS DT data are processed and filtered with the same steps as mentioned in section
268 3.1 to construct $1^\circ \times 1^\circ$ (Latitude/Longitude) monthly averages for trend estimates. MISR products
269 are also binned into monthly-averaged $1^\circ \times 1^\circ$ degree bins and filtered according to Zhang et al.,
270 (2017 submitted).



271 Figure 2 depicts the C6 MODIS Terra (Fig. 2a), C6 MODIS Aqua (Fig. 2b) and v22 MISR
272 (Fig. 2c)-based global aerosol distributions (Latitude: -60° to 60°) using monthly gridded AOTs.
273 Only those bins with more than one thousand data counts were considered for this analysis. A
274 quick comparison between Figs. 2a and 2b shows a high level of similarity over most of the globe,
275 which is consistent with what has been reported by Remer et al. (2006) using 3 years of data.
276 Similar spatial patterns are also found for MODIS- and MISR-based AOT analyses over global
277 oceans (Figure 2c). This is further confirmed from Figures 2d and 2e, which show the ratios and
278 the differences between Terra MODIS and Terra MISR AOTs. Still, the band of high AOT over
279 the southern oceans, which is identified as a potential artifact in both C5 MODIS and MISR aerosol
280 products that may be due to cloud contamination (Toth et al., 2013), is no longer apparent in the
281 C6 MODIS DT aerosol products.

282 Using data shown in Figure 2, the time series of over ocean global mean AOT are also
283 examined and shown in Fig. 3. Figure 3a shows the monthly-averaged C6 MODIS Aqua (red),
284 MODIS Terra (blue) and MISR (green) AOTs over global oceans for the entire time frame of each
285 data set. It should be noted that over land observations from MISR are not included in global
286 averages in order to get a more direct comparison with the over ocean MODIS DT aerosol data
287 sets. Monthly-variations in globally-averaged AOTs can be observed, with the solid lines showing
288 the AOT trends for the entire time period for each sensor. Similar to Zhang and Reid (2010), the
289 lowest monthly-averaged MODIS AOTs are found during the Northern-Hemispheric winter
290 months while the highest aerosol loading activity over global oceans seems to occur during the
291 Northern-Hemispheric spring and summer months.

292 Figure 3b shows AOT anomalies after deseasonalizing the monthly data shown in Figure 3a.
293 Interestingly, Terra MODIS and MISR show trends of differing signs; a statistically significant



294 increase/decrease in monthly-mean AOT values of 0.008/-0.005 AOT decade⁻¹ is found when
295 using Terra MODIS/MISR data for the study period of 2000-2015. In comparison, a statistically
296 insignificant global over ocean AOT trend is found to be 0.0003 AOT decade⁻¹ using Aqua MODIS
297 data for the study period of 2002-2015. A trend difference is clearly seen even if we restrict all
298 datasets to the same study period of 2002-2015, which could be an indication of potential
299 calibration related issues with one or all of the sensors.

300 Zhang and Reid et al., (2010) suggested that since the remote oceans region (defined in Table
301 2) is least affected by major continental originated aerosol plumes, the AOT trend from this region
302 may be used for checking calibration related issues or some other unrealized uncertainties
303 originated from the upstream data used. Similar to Fig. 3b, Fig. 3c depicts the monthly-averaged
304 deseasonalized AOTs over the remote ocean region where the monthly anomalies and trend lines
305 are visible. Similar to Zhang et al. (2017), an insignificant trend of 0.0003 AOT decade⁻¹ is found
306 for the remote ocean region using Aqua MODIS data, while a statistically significant
307 (Weatherhead method) trend of 0.006/-0.004 AOT decade⁻¹ is found for the same region with the
308 use of deseasonalized Terra MODIS/MISR data. Those differences in AOT trends are not
309 surprising. For example, a recent study suggests a potential cross-talk among Terra MODIS
310 thermal channels, which will affect MODIS cloud detection (Moeller and Frey, 2016) and
311 correspondingly, Terra MODIS AOT trends. Similarly, Limbacher and Kahn, (2016) reported an
312 up to 2% decrease in MISR signals from 2002-2014 that could affect MISR AOT trends. AOT
313 trends estimated from this study are henceforth adjusted based on AOT trends detected from the
314 Remote Ocean region; this is done to reduce potential impacts from upstream data used in the AOT
315 retrievals by assuming that a near zero AOT trend should be observed over the remote ocean region
316 (shown in Table 3).



317 Using monthly gridded data, AOT grid-level trends are also estimated on a global scale, for
318 MODIS Terra- (Fig. 1b), MODIS Aqua- (Fig. 1c) and MISR (Fig. 1d)-based analysis for the entire
319 data record period. Again, the black-dotted areas on the map are for regions with statistically
320 significant trends at a 95% confident interval estimated using the WH method. When comparing
321 with the 10-year analysis as mentioned in Section 3.1 (Fig. 1a), some similarities are clearly
322 visible. For example, increasing AOT trends are observed over the Arabian Sea and Indian Bay
323 of Bengal, while decreasing trends are observed over the Mediterranean Sea and east coast of US
324 from both Figures 1a and 1b. Still for some regions, such as over coastal China, Fig. 1a shows a
325 positive AOT trend, yet near zero AOT trend is found in Figure 1b. A recent study suggests a
326 possible increase in AOT from 2000-2007 over coastal China, followed by a decreasing trend from
327 2008-2015 (Zhang et al., 2017), which can be used to explain the differences as observed in Figure
328 1 over coastal China. Likewise, regional analyses are also conducted as documented by Table 3
329 and Figure 4. In addition to the regions reported by Zhang and Reid (2010), two regions have been
330 added to the study which include Persian Gulf (24° N – 30° N, 50° E – 60° E) and Red Sea (15° N
331 – 30° N, 30° E – 45° E). All regions are outlined by black boxes in Fig. 1.

332 Unlike the insignificant AOT trends on the global scale, both statistically significant positive
333 and negative trends are found for several regions as shown in Figure 4 (as well as Table 3). For
334 example, statistically significant positive AOT trends (where statistically significant trends are
335 denoted by bold font on Table 3) are found from all three datasets (Terra and Aqua MODIS DT
336 and MISR over water aerosol products) over the Bay of Bengal (Fig. 4a), Arabian Sea (Fig. 4b)
337 and Red Sea (Fig. 4d). Note that both the Bay of Bengal and Arabian Sea have been identified in
338 Zhang and Reid (2010) as regions with statistically significant positive trends for the study period
339 of 2000-2009. However, the rates of increase of aerosol loading have slowed down over the last



340 five years for both regions, indicated by ~20-30% reductions in AOT trends when estimated using
341 the near full Terra data records. The Red Sea and Persian Gulf are newly introduced for this study
342 but seem to show the highest increase in aerosol loading during the study period (as derived from
343 Terra data). This increase in AOT has been attributed to a number of mechanisms, including a
344 trend in surface wind, precipitation, and soil moisture (Al Senafi and Anis 2015; Klingsmuller et
345 al, 2016), as well as a climatological deepening of the summertime monsoonal low over the
346 Arabian Sea (Solmon et al., 2015). Statistically significant negative trends are found over the
347 Mediterranean Sea (Fig. 4f) and the east coast of N. America (Fig. 4g), again from all three
348 datasets. These findings are also consistent with what has been reported by Toth et al. (2016) with
349 the use of CALIOP data. Also, despite the differences in sampling methods as well as calibration,
350 regional trends from MISR are similar to trends derived using both Aqua and Terra MODIS DT
351 data.

352

353 **4. SWARE Trends**

354 In Section 3, changes in aerosol concentrations over global oceans are studied with respect to
355 AOT trends. The temporal variations in aerosol concentrations could also introduce changes in
356 TOA SW fluxes and thus can be detected using collocated MODIS and CERES (SSF and ES-8)
357 observations. In this section, the SWARE trends derived using MODIS and CERES (SSF and ES-
358 8) data are explored and are inter-compared with AOT trends as mentioned in the previous section.

359

360 **4.1 SWARE trend Analysis using collocated MODIS and CERES data**



361 In several past studies, SWARE values are derived using collocated CERES and MODIS data
362 based on equation 1 (e.g. Loeb and Kato, 2002; Loeb et al., 2003; Zhang et al., 2005b; Christopher
363 and Zhang., 2002a;b):

$$364 \quad SWARE = F_{clear} - F_{aero} \quad (1)$$

365 where F_{clear} represents the TOA SW flux over aerosol and cloud free skies and F_{aero} represents the
366 TOA SW flux over cloud free skies. Taking the derivative of equation 1 with respect to time, we
367 can obtain equation 2:

$$368 \quad \frac{\partial SWARE}{\partial t} = \frac{\partial F_{clear}}{\partial t} - \frac{\partial F_{aero}}{\partial t} \quad (2)$$

369 Here $\partial SWARE/\partial t$ represents the trend in SWARE. $\partial F_{aero}/\partial t$ represents a temporal change in TOA
370 observed SW flux over cloud free skies. $\partial F_{clear}/\partial t$ represents a change in background TOA SW
371 energy over cloud and aerosol free skies. Here F_{clear} is a function of viewing geometry (e.g., solar
372 zenith angle) and near surface wind patterns. By deseasonalizing CERES SW flux data, we can
373 remove the solar zenith angle effect. Also, by using monthly averages of instantaneous retrievals,
374 we assume that there is no viewing zenith or azimuth dependency with respect to time. If we
375 further assume that the changes in near surface wind patterns are negligible for the study period,
376 the $\partial F_{clear}/\partial t$ term can be assumed to be near zero (the impact of near surface wind speed on the
377 SWARE trend is explored in a later section). Thus, we can rewrite equation 2 as:

$$378 \quad \frac{\partial SWARE}{\partial t} = \frac{-\partial F_{aero}}{\partial t} \quad (3)$$

379 As suggested from equation 3, the trends in SWARE can be directly estimated from the temporal
380 variations in SSF/ES-8 TOA SW flux from CERES over cloud free skies (less than 1% cloud
381 fraction and larger than 99% CP). This approach avoids the need for estimating F_{clear} , which cannot
382 be observed and can only be derived through radiative transfer calculations (Christopher, 2011) or
383 extrapolation (e.g., there is always a positive definite AOT).



384 The cloud-free TOA SW fluxes are obtained from CERES (SSF and ES-8) data in this study.
385 This is accomplished by utilizing the collocated MODIS-CERES (SSF and ES-8) data set. As
386 mentioned in Section 2, only those MODIS observations over cloud-free scenes ($CF < 1\%$ and CP
387 $> 99\%$) are used for this analysis as SW flux is sensitive to cloud contamination (Zhang et al.,
388 2005a;b). However, filtering the MODIS data sets with such strict cloud fraction criteria
389 significantly reduces the data volume, which may lead to a sampling bias when working with the
390 MODIS-CERES data set (e.g., Zhang and Reid 2009). Therefore all MODIS-CERES data sets
391 have been averaged into seasons as opposed to monthly averages. In addition, the MODIS-CERES
392 collocated observations are gridded into $2^\circ \times 2^\circ$ (Latitude/Longitude) grids to further alleviate the
393 sampling bias produced by the data reduction in the MODIS-CERES data set.

394 Figure 5 shows the spatial distributions of AOT and cloud-free CERES TOA SW flux over
395 global oceans using collocated MODIS-CERES data (2000-2015 for Terra and 2002-2015 for
396 Aqua). Comparing Figs. 5a and 5b with Figs. 2a and 2b, Terra (5a) and Aqua (5b) AOT plots
397 generated using the collocated MODIS-CERES data are similar to the spatial distributions of AOT
398 generated using the original Terra and Aqua C6 MODIS DT data. Figures 5e and 5f show the
399 gridded cloud-free CERES SSF TOA SW fluxes for Terra and Aqua, respectively. It is interesting
400 to note that the spatial distributions of MODIS AOT and cloud free CERES SSF TOA SW flux
401 (SW_{ssf}), although from two different instruments that measure different physical quantities (narrow
402 band versus broadband energy; dependent versus independent of forward calculations of MODIS),
403 show remarkably similar patterns.

404 Similar to Figs. 5e and 5f, Figs. 5c and 5d show the gridded cloud-free TOA SW fluxes for
405 Terra and Aqua respectively, but with the use of CERES ES-8 SW fluxes. Again, the spatial
406 patterns of cloud-free CERES ES-8 TOA SW flux (SW_{es8}) highly correlate with AOT spatial



407 patterns. Still, an overall difference in CERES SSF and ES-8 TOA SW fluxes is clearly observable
408 (Figs. 5g and 5h) and SW_{ssf} values are generally 8-9 Wm^{-2} higher than SW_{es8} values. Smaller than
409 average differences in cloud free TOA SW fluxes between the two products can be seen over dust
410 aerosol polluted regions such as the northwest coast of Africa, while larger than average
411 differences are found over regions such as east coast of Asia, west coast of South America and
412 Southeast Asia where other type of aerosol particles dominate. For illustrative purposes, data
413 counts for each $2 \times 2^\circ$ (Latitude/Longitude) bin that are used to create Figs. 5a-h are also shown in
414 Figs. 5i and 5j for Aqua and Terra respectively.

415 The relationship between AOT and cloud free TOA SW flux values from Fig. 5 is also
416 evaluated in Figs. 6 and 7 and Table 4. As suggested from Fig. 6a (Aqua) and 6c (Terra), multi-
417 year means of AOTs and SW_{ssf} values share a highly correlated (correlations of 0.72 and 0.73 for
418 Aqua and Terra data, respectively), non-linear relationship. Similar but higher correlations
419 between multi-year mean AOT and SW flux values are also found when using CERES ES-8 data
420 (correlations of 0.83 and 0.87 for Aqua and Terra data, respectively) as shown in Figs. 7a (Aqua)
421 and 7c (Terra).

422 Figure 6b shows the Aqua MODIS AOT and Aqua SW_{ssf} relationship for 5 selected regions
423 that have high regional AOT values (e.g., maximum bin averaged AOT > 0.3), including the
424 southwest and northwest coasts of Africa, coastal China, India Bay of Bengal, and Arabian Sea.
425 In particular, a much lower slope of 37.8 Wm^{-2} per AOT is found for the southwest coast of Africa
426 region in-comparing with the other four regions. A similar pattern is observed for using Terra
427 CERES SSF data (slope of 42.5 Wm^{-2} per AOT for the southwest coast of Africa region) as well
428 as for using both Aqua and Terra CERES ES-8 data (slopes of 39.8 and 43.7 Wm^{-2} per AOT for
429 Aqua and Terra respectively, for the southwest coast of Africa region). Note that the slope of AOT



430 and SW flux is a measure of (inversely proportional to) the instantaneous SW aerosol direct forcing
431 efficiency. Smoke aerosol particles dominate high AOTs for the southwest coast of Africa region,
432 while other regions are also influenced by non-smoke aerosols such as dust aerosol particles. Thus
433 Figs. 6 and 7 suggest a lower SW forcing efficiency (in magnitude) for biomass burning aerosols,
434 in part due to a stronger absorption at the visible spectrum (e.g., Remer et al., 2005).

435 We have further explored the topic by estimating SW aerosol forcing efficiencies for the Dec.-
436 May and Jun.-Nov. seasons as shown in Table 4. As indicated in Table 4, SW aerosol direct
437 forcing efficiencies may experience a seasonal dependency such as over the Coastal China region.
438 For example, a CERES SSF-based aerosol SW forcing efficiency value of -88.3 Wm^{-2} per Aqua
439 MODIS AOT is found for the coastal China region for the Dec.-May period. A lower value
440 (CERES SSF-based) of -74.7 Wm^{-2} per Aqua MODIS AOT is found for the Jun.-Nov. season for
441 the same region. Similar conclusions can also be found using Terra data as well as using CERES
442 ES-8 data. The seasonal dependency in SW aerosol forcing efficiency is not surprising for the
443 coastal China region, as dust aerosols are expected for the spring season, while pollutant and smoke
444 aerosols likely dominate for the Jun.-Nov. study period (Zhang et al., 2017). In comparison, less
445 seasonal-based changes are found for the Arabian Sea region, which may be plausibly linked to
446 less significant temporal variation in aerosol speciation over the region. Also indicated in Table
447 4, the derived SWARE has a strong regional-dependency, while the multi-year averaged SWARE
448 is around -6 to -7 Wm^{-2} for the southwest coast of Africa region, over the coastal China region,
449 SWARE values of below -20 Wm^{-2} are found. Note that this conclusion remains unchanged
450 regardless of using Terra or Aqua data, or using CERES ES-8 or SSF ADMs.

451 Over global oceans, the multi-year mean instantaneous SW aerosol direct forcing efficiencies
452 are estimated to be -61 (-58) and -58 (-58) Wm^{-2} per AOT using Aqua and Terra CERES SSF (ES-



453 8) data, respectively. Those numbers are lower than -70 Wm^{-2} per AOT, which is reported from a
454 previous study (Christopher and Jones, 2008). We suspect that the differences in forcing efficiency
455 values may be introduced by different data screening methods as well as a much longer study
456 period. Still, using estimated forcing efficiencies as well as AOTs (Table 4), the global mean (14
457 years of Aqua and 16 years of Terra data) over oceans SWARE values are found to be around -7
458 Wm^{-2} regardless of datasets (Terra or Aqua) and ADMs (SSF or ES-8) used. Note that regional
459 and global mean AOTs as shown in Table 4 are derived using the collocated MODIS and CERES
460 datasets, representing mean AOTs over CERES cloud-free skies. Thus, mean AOTs as reported
461 from Table 4 are different from AOTs as included in Table 2.

462 With the use of seasonally gridded SW flux values, the times series of cloud-free sky CERES
463 SSF and ES-8 TOA SW flux over global oceans are investigated and depicted in Fig. 8a, and the
464 corresponding deseasonalized cloud-free sky flux anomalies are show in Fig. 8b. While Fig. 8a
465 suggests an $\sim 8 \text{ Wm}^{-2}$ difference in mean over ocean cloud-free sky SW flux between CERES SSF
466 and ES-8 products, a small difference in cloud-free sky SW flux trend of $0.2\text{-}0.3 \text{ Wm}^{-2} \text{ decade}^{-1}$ is
467 found (Fig. 8b) between the two products for both Terra and Aqua data. For example, negative
468 trends on the order of -0.50 Wm^{-2} and -0.26 Wm^{-2} per decade are found for using Aqua CERES
469 ES-8 and SSF products respectively. Also, although larger cloud-free sky SW flux trends in
470 magnitude are found when using Terra data, the difference between CERES SSF-based and
471 CERES ES-8-based trends is still on the order of $0.2 - 0.3 \text{ Wm}^{-2} \text{ decade}^{-1}$ (Cloud-free sky SW flux
472 trend is $-1.50 \text{ Wm}^{-2} \text{ decade}^{-1}$ for Terra CERES ES-8 data and is $-1.22 \text{ Wm}^{-2} \text{ decade}^{-1}$ for Terra
473 CERES SSF data). Figures 8a and 8b may imply that different ADMs could significantly impact
474 the derived SW flux values, but their impact on cloud-free sky TOA SW flux trends are rather
475 marginal.



476 Similar to Section 3, we used CERES SW flux trends over the remote ocean region as
477 indicators for potential radiometric calibration related issues. The deseasonalized CERES SSF
478 (ES-8) SW trends over the remote ocean regions (Fig. 8c) seem to suggest plausible artificial trends
479 of -0.25 (-0.50) $\text{Wm}^{-2} \text{decade}^{-1}$ for Aqua and -0.70 (-0.92) $\text{Wm}^{-2} \text{decade}^{-1}$ for Terra, although these
480 trends are also affected by various uncertainties that are further explored in a later section. To
481 examine if we could observe similar issues with the use of full CERES SSF / ES-8 datasets, Fig.
482 9 shows the all sky CERES flux trend for the same study periods as Fig. 8. Decadal changes of
483 SSF (ES-8) all sky flux are less than $0.5(0.7) \text{Wm}^{-2}$ and $0.4(0.5) \text{Wm}^{-2}$ for Terra and Aqua data,
484 respectively. The Aqua all-sky flux trends are comparable to cloud-free sky trends for both SSF
485 and ES-8 fluxes. However Terra-based all sky trends are much lower in magnitude than the
486 corresponding cloud-free flux, which indicates that cloud-free sky CERES SW energy may be
487 more sensitive to calibration related issues than all sky flux data for Terra-based analysis only.
488 Still, if we account for the changes in SW trends over the remote ocean region, a negligible SW
489 flux (SWARE) trend for Aqua and a negative (positive) SW flux (SWARE) trend of -0.5Wm^{-2}
490 decade^{-1} ($0.5 \text{Wm}^{-2} \text{decade}^{-1}$) for Terra can be estimated for the global oceans from collocated
491 MODIS-CERES data.

492 Surprisingly, although different cloud-free sky SW flux trends are found while using CERES
493 ES-8 data, after adjusting the detected trends with trends from remote oceans, a zero SW flux
494 (SWARE) trend is found while using collocated Aqua ES-8 SW fluxes from the MODIS-CERES
495 data and a negative (positive) SW flux (SWARE) trend of $-0.6 \text{Wm}^{-2} \text{decade}^{-1}$ ($0.6 \text{Wm}^{-2} \text{decade}^{-1}$)
496 is found using collocated Terra ES-8 SW fluxes from the MODIS-CERES collocated data, both
497 are in good agreement with values estimated using the SSF SW fluxes from the same data. This



498 again may seem to suggest that the impact of ADMs on SWARE trends over global oceans
499 estimated from the collocated MODIS and CERES data are rather marginal.

500 A regional trend analysis for the deseasonalized cloud-free sky SSF and ES-8 SW fluxes is
501 also carried out and presented in Table 3 and Figure 10. A good agreement is shown between
502 regional trends of AOTs (Fig. 4) and cloud-free fluxes (Fig. 10) for a majority of the regions (also
503 shown in Table 3 for a direct comparison). For example, statistically significant positive (based
504 on the Mann-Kendall method) SW flux trends are found over the Arabian Sea, and statistically
505 significant negative trends are found over the Mediterranean Sea and eastern US coast for both
506 Aqua and Terra-based analyses. Also, over the east coast of China, although a near positive trend
507 is found for the study period of 2000-2008 (Terra), the SW flux trend turns negative from 2009-
508 2015 (Figure 11). This is consistent with what has been reported for AOT trends from a recent
509 study (Zhang et al., 2017) as well as in Section 3. For regions such as the Bay of Bengal, although
510 positive SW flux trends are found, the trends are not statistically significant for one or all datasets.

511 Next, the grid-level AOT and cloud-free flux trends are derived from the collocated
512 MODIS-CERES data sets as shown in Fig. 12. Figures 12a (Terra) and 12b (Aqua) depict the de-
513 biased (applied corrections based on the estimate from the remote ocean region) changes in
514 deseasonalized AOT per year for each $4^{\circ}\times 4^{\circ}$ (Latitude/Longitude) grid (averaged from the $2^{\circ}\times 2^{\circ}$
515 Latitude/Longitude dataset) over the entire time period (all seasons and years combined). Figures
516 12e and 12f depict the grid level CERES SSF SW flux trends over cloud-free skies similar to Figs.
517 12a and 12b. Similar to the AOT grid level analysis shown in Fig. 1, at least 60 percent of the data
518 record in each grid are required to have valid AOT and SW flux trend values. Comparing between
519 Aqua AOT (Fig. 12b) and CERES SSF cloud free SW (Fig. 12f) trends, similarity can be found.
520 For example, positive trends are found, from both plots, over coastal Indian and the Arabian Sea



521 regions, and negative trends are observable from Europe and the east coast of North America. The
522 similar conclusion can also be reached when using Terra data (Figs. 12a and 12e) as well as when
523 using CERES ES-8 data (Figs. 12c and 12d). Still discrepancies can be found. For example,
524 although the spatial distributions of AOT from both Terra and Aqua show similar patterns,
525 differences between the spatial distributions of Terra and Aqua CERES cloud-free SW fluxes,
526 regardless of ADMs used, are clearly visible. Much larger regions with negative cloud free SW
527 flux trends are found for using Terra data. This may be a result of several possible issues such as
528 SW flux outliers in the CERES data set, quality control applied to the CERES data set, or cloud
529 contamination issues. Thus, this will be examined in the following section.

530

531 **4.2 Uncertainty in Cloud-Free Flux Trend Analysis**

532 In this section, issues that could impact the derived SWARE trends are explored, which
533 include changes in near surface wind patterns, cloud contamination, and uncertainties in the cloud
534 free SW flux trend estimates over the remote ocean region (used as a proxy for radiometric
535 calibration). Note that there are other uncertainty sources that may impact the derived CERES SW
536 flux values, such as uncertainties in converting unfiltered to filtered radiances (Zhang et al.,
537 2005b). However, temporal variations of those uncertainty sources are assumed to be negligible
538 for this study, and thus those terms are not included in the trend uncertainty analysis.

539 *4.2.1 Baseline region (a proxy for radiometric calibration):* As mentioned in Section 4.1, the TOA
540 cloud-free SW flux trend over the Remote Ocean region is used as an indicator for potential
541 calibration related issues. The selection of the Remote Ocean region boundaries is rather arbitrary,
542 and thus the variations in TOA cloud-free CERES SW flux trends over the remote ocean region
543 are investigated by modifying the regional boundaries for four different scenarios as shown in



544 Table 5. Alternate remote ocean regions are chosen by shifting the original boundaries by 10
545 degrees in each direction. The variations in estimated CERES SSF (ES-8) SW flux trends, which
546 correspond to standard deviation values of 0.08 (0.09) and 0.03 (0.08) $\text{Wm}^{-2} \text{decade}^{-1}$ for Terra and
547 Aqua, respectively, provide the first order estimation of the potential variations in the estimated
548 SW trends over the remote oceans.

549 *4.2.2 Cloud fraction:* Similarly, the cloud-free SW flux trends over global oceans are estimated
550 through varying MODIS cloud fractions from 0 to 5% as indicated in Table 5. The standard
551 deviation of the data spread is found to be less than 0.1 $\text{Wm}^{-2} \text{decade}^{-1}$ for both Terra- and Aqua-
552 based CERES SSF and ES-8 SW flux trend analyses, suggesting that cloud contamination has a
553 minor effect on the trend analysis. This conclusion is also confirmed by a sensitivity test by
554 estimating SSF and ES-8 SW flux trends through varying CP values from 95% to 100%.

555 *4.2.3 Thin Cirrus:* Through the use of CALIOP observations, several studies suggest that OTC
556 cloud contamination exists in MODIS detected totally cloud free skies (e.g., Toth et al., 2013).
557 Therefore, the impacts of OTC clouds are evaluated by collocating CALIOP cloud layer data with
558 the already collocated Aqua MODIS and CERES data pairs. All CALIOP observations are
559 spatiotemporally collocated with the current original CERES observation if the temporal
560 difference in the two sensor's scan times is less than or equal to five minutes and if the center of
561 the CALIOP observations lies within 0.3 degrees of the center of the CERES observations. All
562 collocated CERES observations are assigned a cirrus cloud flag depending on whether any of the
563 collocated CALIOP pixels was found to be contaminated by cirrus clouds. The global averaging
564 process is once again performed using the collocated MODIS-CERES-CALIOP observations.
565 CERES observations which are contaminated by cirrus clouds, as identified by CALIOP data, are
566 removed from the averaging process. The resulting global AOT and cloud-free flux trends are



567 presented in Figs. 13a and 13b, respectively for using both CERES ES-8 and SSF SW fluxes. For
568 comparison, the MODIS-CERES trends are also shown (red) over the same time period (summer
569 2006 – fall 2015). Despite differences in globally averaged AOTs, the global TOA SW flux trends
570 derived using the two different data sets are remarkably similar. The standard deviation in global
571 cloud-free CERES SSF flux trend calculations due to OTC is less than $0.1 \text{ Wm}^{-2} \text{ decade}^{-1}$, as shown
572 in Table 5. Thus, OTC clouds may have a minimal impact on the derived cloud-free SW flux
573 trends.

574 *4.2.4 Surface Wind and ADMs:* The uncertainty in cloud-free SW flux trends are also examined as
575 a function of surface wind speeds and ADMs. As mentioned previously, the effect of surface wind
576 speed is included in CERES ADMs (used in the SSF data set). Thus, the SWARE trends derived
577 from the CERES SSF datasets are used to investigate ADMs and surface wind speed related
578 uncertainties in this study. Based on Table 3, the cloud-free sky SW flux trends derived from the
579 CERES SSF SW flux are -0.26 and $-1.22 \text{ Wm}^{-2} \text{ decade}^{-1}$ for using Aqua and Terra datasets
580 respectively, and the numbers are -0.50 and $-1.50 \text{ Wm}^{-2} \text{ decade}^{-1}$ for using CERES ES-8 data.
581 Thus, the cloud-free SW flux trends derived using the CERES ES-8 are on the order of -0.25 Wm^{-2}
582 decade^{-1} (corresponding to standard deviation values of 0.20 and $0.17 \text{ Wm}^{-2} \text{ decade}^{-1}$ for Terra
583 and Aqua, respectively) lower than the same trends derived using CERES SSF data for the same
584 study period. The $\sim 0.25 \text{ Wm}^{-2} \text{ decade}^{-1}$ difference indeed contains combined uncertainties from
585 ADMs as well as the changes in surface wind speeds for both Terra and Aqua datasets.

586 Overall, the largest sources of uncertainty in the SWARE trend estimates are from ADMs
587 / near surface wind speed changes while the impact of cloud contamination is rather minor. If we
588 assume the standard deviation values from Table 5 can be considered as uncertainties, an overall



589 uncertainty in the trend analysis can be estimated based on equation 4 (Penner et al., 1994; Zhang
590 et al., 2005b):

$$591 \quad U_t = e^{[\sum \log U_i^2]^{0.5}} \quad (4)$$

592

593 Where U_t is the overall uncertainty factor and U_i is the uncertainty factor from each item
594 in Table 5. The uncertainty factor is defined as such that if the percentage uncertainty is 8%, then
595 the uncertainty factor is 1.08. As shown in Table 5, estimated from Equation 4, the overall
596 uncertainties for the SWARE trends estimated using CERES SSF data are 0.3 and 0.2 Wm^{-2}
597 decade^{-1} for Terra and Aqua based analyses respectively, shown also in Table 5. Note that similar
598 numbers are also found by repeating the same exercise but using CERES ES-8 data as shown in
599 Table 5.

600

601 **5. Comparison to other aerosol related trend analyses**

602 Both AOT and SWARE trends are estimated in this study. Using CALIOP data from 2006-
603 2014, Toth et al. (2016) studied AOT and aerosol vertical distribution trends over both land and
604 oceans. Alfaro-Contreras et al. (2016) explored temporal variations in above cloud AOT with the
605 combined use of Ozone Monitoring Instrument (OMI) and CALIOP data. Although different
606 spectral widths (narrowband versus broadband), different instruments (passive versus active
607 sensors) and different observing conditions (cloud-free skies versus cloudy skies) are considered
608 in different studies, it is interesting to inter-compare trends derived from those studies, as shown
609 in Table 6. Another reason for selecting these studies is because AOT trends for similar regions
610 are reported.



611 Four studies are listed in Table 6, including passive based AOT analysis (Zhang and Reid 2010;
612 this study); SWARE analysis (this study); CALIOP-based AOT analysis (Toth et al., 2016); and
613 above-cloud AOT analysis (Alfaro-Contreras et al., 2016). It should be noted that only over ocean
614 data are used for the studies utilizing passive-based instruments (Zhang and Reid, 2010; current
615 study). The estimated trends from the active-based studies (Alfaro-Contreras et al., 2016; Toth et
616 al., 2016) included both land and ocean CALIOP data. Also, different data sampling, data
617 screening, and filtering methods are applied for different studies.

618 Table 6 includes estimates for global oceans for 7 selected regions that have reported values
619 from all four studies. It is interesting to note that positive trends in AOT (both from passive and
620 active methods), SWARE, and above cloud AOT are found over the Bay of Bengal and Arabian
621 Sea, although trends from some analyses are insignificant such as from the above cloud AOT
622 analysis (Alfaro-Contreras et al., 2016). Negative trends are found, across all four studies, over
623 the Mediterranean Sea and eastern coast of the US. The cohesive results from studies using
624 different instruments with varying methods, seem to add more fidelity to the trend analysis of this
625 study.

626 Still, over coastal China, while Zhang and Reid (2010) reported a statistically significant
627 positive AOT trend for the study period of 2000-2009, negative AOT trends are found from both
628 this study (2000-2015) and Toth et al., (2016; for 2006-2014). Again, this is because a potential
629 increase in aerosol loading for the early study period (2000-2007) continued with a decreasing
630 trend in aerosol loading after 2008, as suggested by a recent study (Zhang et al., 2017).

631

632 **6. Summary and Conclusions**



633 Using Terra (2000-2015) and Aqua (2002-2015) Collection 6 (C6) Moderate Resolution and
634 Imaging Spectroradiometer (MODIS) Dark Target (DT), Multi-angle Imaging Spectroradiometer
635 (MISR; 2000-2015) and Cloud and Earth's Radiant Energy System (CERES) ES-8/SSF data, both
636 Aerosol Optical Thickness (AOT) and Short-Wave Aerosol Radiative Effect (SWARE) trends are
637 estimated over global oceans. The results of this study are inter-compared with analyses from
638 several other studies that derived AOT trends using different instruments (e.g. active versus
639 passive) over different observing scenes (e.g. cloudy versus cloud free). This study suggests:

- 640 1. Updating the analysis from Zhang and Reid (2010), which examined AOT trend over
641 global oceans using the Collection 5 (C5) Terra MODIS DT aerosol data for 2000-2009,
642 the use of the newly released C6 Terra MODIS DT aerosol products introduces a marginal
643 differences in derived global and regional AOT trends.
- 644 2. Using the near full data record from Terra (2000-2015), Aqua (2002-2015), and MISR
645 (2000-2015), global and regional AOT trends are derived using over ocean C6 MODIS DT
646 and MISR data. A negligible AOT trend ($0.0003 \text{ AOT decade}^{-1}$) is found using Aqua C6
647 MODIS DT data, but a higher AOT trend of $0.008 \text{ AOT decade}^{-1}$ is found using Terra C6
648 MODIS DT data, while a slight negative trend is derived using MISR data (-0.005 AOT
649 decade^{-1}). It is suspected that the difference may be introduced by calibration related issues
650 for one or all sensors, such as the recently reported cross-talk in thermal channels for Terra
651 MODIS (Moeller and Frey, 2016), and a slight decrease in signal sensitivity for Terra
652 MISR (Limbacher and Kahn, 2016). After accounting for potential calibration drifts,
653 negligible AOT trends are found over global oceans using data from all sensors.
- 654 3. Regionally, statistically significant increases in aerosol loading over time are found over
655 regions such the Indian Bay of Bengal, Arabian Sea, and the Red Sea. Statistically



656 significant negative AOT trends are also found over the eastern US coast and
657 Mediterranean Sea. This is in agreement from all three sensors (MODIS Aqua, MODIS
658 Terra and MISR).

659 4. Using collocated MODIS and CERES data over global oceans, the SW flux (*SWARE*)
660 trends are also estimated for the near-full Terra (2000-2015) and Aqua (2002-2015) data
661 records. After accounting for the potential calibration / angular distribution models
662 (ADMs) / near surface wind related issues, small negative (*positive*) trends of -0.5 to -0.6
663 $\text{Wm}^{-2} \text{decade}^{-1}$ ($0.5 - 0.6 \text{ Wm}^{-2} \text{decade}^{-1}$) are found for Terra based analysis and a near zero
664 trend is found for using Aqua data, and the results are rather consistent regardless of using
665 CERES SSF or ES-8 SW fluxes. Regionally, positive SW flux trends are found over
666 regions such as the Bay of Bengal and Arabian Sea, where statistically significant negative
667 trends are found over the eastern US coast and Mediterranean Sea. The signs of the
668 regional SW flux trends are in good agreement to what has been found for AOT trends.

669 5. Very high correlations are found between MODIS DT AOT and CERES cloud-free SW
670 flux values using $2 \times 2^\circ$ (Latitude/Longitude) gridded multi-year mean Terra (2000-2015)
671 and Aqua (2002-2015) data. The SW aerosol direct forcing efficiency is estimated to be -
672 60 Wm^{-2} per AOT and a *SWARE* value of -7 Wm^{-2} is derived over global oceans. The
673 results are consistent, regardless of using Terra or Aqua data, or using of CERES ES-8 or
674 SSF data. Regionally, over the southwest coast of Africa, where smoke aerosol particles
675 dominate in summer months, a SW aerosol direct forcing efficiency value of $\sim -40 \text{ Wm}^{-2}$
676 per AOT is found, again, regardless of datasets used. SW aerosol direct forcing efficiency
677 values of -50 to -80 Wm^{-2} per AOT are also found for Arabian Sea, northwest coast of



678 Africa, coastal China and Indian Bay of Bengal, where dust and pollutant aerosols
679 dominate.

680 6. Factors that could impact SWARE trend analysis include cloud contamination, calibration
681 drifts, ADMs, ocean wind patterns, and optically thin cirrus (OTC) clouds. The largest
682 sources of uncertainty in the derived SWARE trends are found to be related to
683 ADMs/surface wind speeds, while cloud contamination has a minor impact on the
684 estimated SWARE trends.

685 7. Finally, trend analyses from this study are inter-compared with results from several
686 selected studies (e.g., Zhang and Reid, 2010; Alfaro-Contreras et al, 2016; Toth et al.,
687 2016). Consistency in increasing/decreasing AOT trends is found among the studies, using
688 passive and active based instruments, over cloud free and cloudy skies, as well as using
689 narrowband and broadband observations over regions such as the Bay of Bengal, Arabian
690 Sea, the eastern US coast and Mediterranean Sea. This study suggests that comprehensive
691 observational systems can and should be used in future studies to gain a better
692 understanding of any changes in atmospheric aerosol states.

693

694

695

696

Acknowledgments

697 Author RC acknowledges the support from a NASA project NNX14AJ13G and a NSF project
698 IIA-1355466. Author J. Zhang also acknowledges the support from an ONR 32 project N00014-
699 16-1-2040 (Grant 11843919). Author JS Reid was supported by ONR 32 project
700 N00014-16-1-2040

701

702



703 **References**

704 Alfaro-Contreras, R., Zhang, J., Campbell, J.R., and Reid, J.S.: Investigating the frequency and
705 interannual variability in global above-cloud aerosol characteristics with CALIOP and
706 OMI, *Atmos. Chem. Phys.*, 16, 47-69, 2016.

707 Al Senafi, F., and Anis, A.: Shamals and climate variability in the Northern Arabian/Persian Gulf
708 from 1973-2012, *Int. J. Climo.*, 35, 4509-4528, doi: 10.1002/joc.4302, 2015.

709 Barkstrom, B.R., and Wielicki, B.A.: Cloud and the Earth's Radiant Energy System (CERES)
710 Algorithm and Theoretical Basis Document: CERES Data Processing Objectives and
711 Architecture (Subsystem 0), 1996.

712 Christopher, S. A.: Satellite remote sensing methods for estimating clear Sky shortwave Top of
713 atmosphere fluxes used for aerosol studies over the global oceans, *Remote Sensing of*
714 *Environment*, doi:10.1016/j.rse.2011.06.003, 2011.

715 Christopher, S. A., and Zhang, J.: Daytime variation of shortwave direct radiative forcing of
716 biomass burning aerosols from GOES 8 imager, *J. Atmos. Sci.*, 59(2), 681–691, 2002a.

717 Christopher, S. A., and Zhang, J.: Shortwave aerosol radiative forcing from MODIS and CERES
718 observations over the oceans, *Geophys. Res. Lett.*, 29(18), 1859,
719 doi:10.1029/2002GL014803, 2002b.

720 Christopher, S. A., and Jones, T. A.: Short-wave aerosol radiative efficiency over the global oceans
721 derived from satellite data, *Tellus B*, 60, 636–640. doi:10.1111/j.1600-0889.2008.00353.x,
722 2008.

723 Diner, D.J., Beckert, J.C., Bothwell, G.W., and Rodriguez, J.I.: Performance of the MISR
724 instrument during the first 20 months in Earth orbit, *IEEE T. Geosci. Remote Sens.*,
725 40(7),1449-1466, 2002.



- 726 Geier, E. B., Green, R. N., Kratz, D.P., Minnis, P., Miller, W.F, Nolan, S.K., and Franklin, C.B.:
727 Single satellite footprint TOA/surface fluxes and clouds (SSF) collection document, cited
728 2003. [http://ceres.larc.nasa.gov/documents/collect_guide/pdf/SSF_CG_R2V1.pdf].
- 729 Hsu, N. C., Gautam, R., Sayer, A. M., Bettenhausen, C., Li, C., Jeong, M. J., Tsay, S.-C., and
730 Holben, B. N.: Global and regional trends of aerosol optical depth over land and ocean
731 using SeaWiFS measurements from 1997 to 2010, Atmos. Chem. Phys., 12, 8037-8053,
732 doi:10.5194/acp-12-8037-2012, 2012.
- 733 IPCC: Climate Change 2013: The Physical Science Basis: Summary for Policymakers,
734 Cambridge, UK, 2013.
- 735 Kahn, R. A., Gaitley, B. J., Garay, M. J., Diner, D. J., Eck, T., Smirnov, A., and Holben, B. N.:
736 Multiangle Imaging Spectroradiometer global aerosol product assessment by comparison
737 with Aerosol Robotic Network. J. Geophys. Res., Vol. 115, D23209, doi:
738 10.1029/2010JD014601, 2010.
- 739 Kato, S., Rose, F.G., Sun-Mack, S., Walter, F.M., Chen, Y., Rutan, D.A., Stephens, G.L., Loeb,
740 N.G., Minnis, P., Wielicki, B.A., Winker, D.M., Charlock, T.P., Stackhouse, P.W., Xu, K.-
741 M., and Collins, W.D.: Improvements of top-of-atmosphere and surface irradiance
742 computations with CALIPSO-, CloudSat-, and MODIS-derived cloud and aerosol
743 properties, J. Geophys. Res., 116, D19209, doi:[10.1029/2011JD016050](https://doi.org/10.1029/2011JD016050), 2011.
- 744 Kendall, M.G.: Rank Correlation Methods. Griffin: London, 1975.
- 745 Klingmüller, K., Pozzer, A., Metzger, S., Stenchikov, G. L., and Lelieveld, J.: Aerosol optical
746 depth trend over the Middle East, Atmos. Chem. Phys., 16, 5063-5073, doi:10.5194/acp-
747 16-5063-2016, 2016.



- 748 Levy, R.C., Mattoo, S., Munchak, L.A., Remer, L.A., Sayer, A.M., Patadia, F., Hsu, N.C.: The
749 Collection 6 MODIS aerosol products over land and ocean, *Atmos. Meas. Tech.*, 6, 2989–
750 3034, doi:10.5194/amt-6-2989-2013, 2013.
- 751 Li, J., Carlson, B.E., Dubovik, O., and Lacis, A.A.: Recent trends in aerosol optical properties
752 derived from AERONET measurements, *Atmos. Chem. Phys.*, 14, 12271–12289, doi:
753 10.5194/acp-14-12271-2014, 2014.
- 754 Loeb, N. G., and Kato, S.: Top-of-atmosphere direct radiative effect of aerosols from the Clouds
755 and the Earth's Radiant Energy System (CERES) satellite instrument, *J. Clim.* 15, 1474–
756 1484, 2002.
- 757 Loeb, N. G., Smith, N. M., Kato, S., Miller, W.F., Gupta, S.K., Minnis, P., and Wielicki, B.A.:
758 Angular distribution models for top-of-atmosphere radiative flux estimation from the
759 Clouds and the Earth's Radiant Energy System instrument on the Tropical Rainfall
760 Measuring Mission Satellite. Part I: Methodology. *J. Appl. Meteor.*, 42, 240–266, 2003.
- 761 Limbacher, J. A., and Kahn R. A.: Updated MISR Dark-Water Research Aerosol Retrieval
762 Algorithm – Part 1: Empirical Calibration Corrections and Coupled 1.1 km Ocean-Surface
763 Chlorophyll-a Retrievals, *Atmos. Meas. Tech. Discuss.*, doi:10.5194/amt-2016-360, in
764 review, 2016.
- 765 Mann, H.B.: Nonparametric tests against trend. *Econometrica* 13: 245–259, 1945.
- 766 Moeller C., and Frey R.: Impact of Terra/MODIS PV LWIR cross talk on L1 and L2 Products,
767 The MODIS Science Team Meeting, June 6 – June 10, 2016, Silver Spring, MD, 2016.
- 768 Penner, J. E., Charlson, R.J., Schwartz, S.E., Hales, J.M., Laulainen, N.S., Travis, L., Leifer, R.,
769 Novakov, T., Ogren, J., and Radke, L.F.: Quantifying and minimizing uncertainty of
770 climate forcing by anthropogenic aerosols, *Bull. Am. Meteorol. Soc.*, 75, 375– 400, 1994.



771

772

773 Remer L. A., Kaufman Y. J., Tanré D., Mattoo S., Chu D. A., Martins J. V., Li R. R., Ichoku C.,
774 Levy R. C., Kleidman R. G., Eck T. F., Vermote E., and Holben B. N.: The MODIS aerosol
775 algorithm, products, and validation, *J. Atmos. Sci.*, 62, pp. 947–973, doi:
776 <http://dx.doi.org/10.1175/JAS3385.1>, 2005.

777 Remer, L. A., Kaufman, Y. J., and Kleidman, R. G.: Comparison of three years of Terra and Aqua
778 MODIS Aerosol Optical Thickness Over the Global Oceans. *IEEE, Geosci. Remote Sens.*
779 *Lett.*, 3(4), 537–540, 2006.

780 Shi, Y., Zhang, J., Reid, J. S., Holben, B., Hyer, E. J., and Curtis, C.: An analysis of the collection
781 5 MODIS over-ocean aerosol optical depth product for its implication in aerosol
782 assimilation, *Atmos. Chem. Phys.*, 11, 557–565, doi:10.5194/acp-11-557-2011, 2011.

783 Solmon, F., Nair, V. S., and Mallet, M.: Increasing Arabian dust activity and the Indian summer
784 monsoon, *Atmos. Chem. Phys.*, 15, 8051–8064, doi:10.5194/acp-15-8051-2015, 2015.

785 Suttles, J. T., Green, R.N., Minnis, P., and Stowe, L.L: Angular radiation models for Earth-
786 atmosphere system. I—Shortwave radiation, Rep. NASA RP-1184, 144 pp., NASA,
787 Greenbelt, Md., 1988.

788 Toth T.D., Zhang, J., Campbell J.R., Reid, J.S., Shi. Y, Johnson, R.S., Smirnov, A., Vaughan, M.
789 A., and Winker, D.M.: Investigating enhanced Aqua MODIS aerosol optical depth
790 retrievals over the mid-to-high latitude Southern Oceans through intercomparison with co-
791 located CALIOP, MAN, and AERONET data set, *J. Geophys. Res. Atmos.*, 118, 4700-
792 4714, doi:10.1002/jgrd.50311, 2013.



- 793 Toth, T.D., Zhang, J., Campbell, J.R., Reid, J.S., and Vaughan, M.A.: Temporal variability of
794 aerosol optical thickness vertical distribution observed from CALIOP, *J. Geophys. Res.*
795 *Atmos.*, 121, doi:10.1002/2015JD024668, 2016.
- 796 Weatherhead, E. C., Reinsel, G. C., Tiao, G. C., Meng, X. L., Choi, D., Cheang, W. K., Keller, T.,
797 DeLuisi, J., Wuebbles, D. J., Kerr, J. B., Miller, A. J., Oltmans, S. J. and Frederick, J. E.:
798 Factors affecting the detection of trends: statistical considerations and applications to
799 environmental data, *J. Geophys. Res.*, 103, 17149– 17161, 1998.
- 800 Wielicki, B. A., Barkstrom, B.R., Harrison E.F., Lee III, R.B., Smith G.L., and Cooper, J.E.:
801 Clouds and the Earth’s Radiant Energy System (CERES): An Earth Observing System
802 Experiment, *Bull. Am. Meteorol. Soc.*, 77, 853–868, 1996.
- 803 Winker, D. M. and coauthors.: The CALIPSO mission: a global 3D view of aerosols and clouds,
804 *B. Am. Meteorol. Soc.*, 91, 1211–1229, 2010.
- 805 Zhang, J., and Christopher S. A.: Longwave radiative forcing of Saharan dust aerosols from Terra,
806 *Geophys. Res. Lett.*, 30 , 2188, doi:10.1029/2003GL018479, 2003.
- 807 Zhang, J. and Reid, J.S.: MODIS aerosol product analysis for data assimilation: Assessment of
808 level 2 aerosol optical thickness retrievals, *J. Geophys.*
809 *Res.*, 111, D22207, doi:10.1029/2005JD006898, 2006.
- 810 Zhang J., and Reid, J. S.: An analysis of clear sky and contextual biases using an operational over
811 ocean MODIS aerosol product, *Geophys. Res. Lett.*, 36, L15824,
812 doi:10.1029/2009GL038723, 2009.
- 813 Zhang, J., and Reid, J.S.: A decadal regional and global trend analysis of the aerosol optical depth
814 using data assimilation grade over-water MODIS and Level 2 MISR aerosol products,
815 *Atmos. Chem. Phys.*, 10, 10949-10963, doi:10.5194/acp-10-10949-2010, 2010.



- 816 Zhang, J., Christopher, S.A., Remer, L.A., and Kaufman, Y.J.: Shortwave aerosol radiative forcing
817 over cloud-free oceans from Terra: 1. Angular models for aerosols, *J. Geophys. Res.*,
818 *D10S23*, doi:10.1029/2004JD005008., 2005a.
- 819 Zhang, J., Christopher, S.A., Remer, L.A., and Kaufman, Y.J.: Shortwave aerosol radiative forcing
820 over cloud-free oceans from Terra: 2. Seasonal and global distributions, *J. Geophys. Res.*,
821 *D10S24*, doi:10.1029/2004JD005009, 2005b.
- 822 Zhang J., Reid, J. S., Alfaro-Contreras, R., and Xian P.: Has China been exporting less air pollution
823 over the past decade?, *Geophysical Research Letters*, DOI: 10.1002/2017GL072617, 2017.
824



825 Table 1. List of datasets used in the study.

Datasets	Study periods	Purposes
C6 Aqua MODIS DT	July 2002- Dec. 2015	AOT trend, cloud fraction
C6 Terra MODIS DT	Mar. 2000 - Dec. 2015	AOT trend, cloud fraction
Terra MISR	Mar. 2000 - Dec. 2015	AOT trend
C6 Aqua CERES-ES-8-SSF	July 2002 - Dec. 2015	Cloud free SW flux trend
C6 Terra CERES-ES-8-SSF	Mar. 2000 - Dec. 2015	Cloud free SW flux trend
CALIOP	June 2006 - Nov. 2015	Thin cirrus cloud mask



826 Table 2. AOT trend analysis for global and selected regions as suggested from Zhang and Reid, 2010. Both trends from Collection 5
 827 (C5, Zhang and Reid, 2010) and Collection 6 (C6) over-water Terra MODIS AOT data are shown for the study period of 2000-2009.
 828 The trend significances are derived using two different methods ($|\omega/\sigma_\omega|$ and $|z|$ values as estimated from the Weatherhead and Mann-
 829 Kendall methods, respectively). The corrected slopes refer to the slopes after accounting for the slope changes over the Remote Ocean
 830 region. AOT trend and trend significances for C5 MODIS DT data are obtained from Zhang and Reid, (2010), which are derived
 831 using Data-assimilation Quality C5 MODIS DT data. For illustration purposes, C5* and C6 Terra MODIS AOT values, derived using
 832 similar methods as mentioned in this study, are also listed. C5* MODIS DT AOTs listed here are not from the Data-assimilation
 833 quality products as used in Zhang and Reid (2010).

Region	Latitude	Longitude	Slope AOT/ decade Terra		Trend Significance (Terra)		Corrected Slope AOT/decade (Terra)		Mean AOT (Terra)	
			C5	C6	C5 $ \omega/\sigma_\omega $	C6 $ \omega/\sigma_\omega $	C5	C6	C5*	C6
Global			0.010	0.011	3.60	4.85	0.003	0.005	0.154	0.140
Africa (NW Coast)	8°N - 24°N	60°W - 18°W	-0.006	-0.004	0.61	0.37	-0.013	-0.010	0.247	0.257
Bay of Bengal	10°N - 25°N	78°E - 103°E	0.076	0.074	5.63	4.79	0.069	0.068	0.319	0.326
Coastal China	20°N - 40°N	110°E - 125°E	0.069	0.086	4.06	4.69	0.062	0.080	0.460	0.462
Central America	5°N - 20°N	120°W - 90°W	-0.016	-0.011	1.73	1.12	-0.023	-0.017	0.151	0.165
Arabian Sea	5°N - 23°N	50°E - 78°E	0.065	0.077	5.40	4.95	0.058	0.071	0.319	0.329
Mediterranean Sea	30°N - 45°N	0° - 40° E	-0.009	-0.009	0.94	0.96	-0.016	-0.015	0.200	0.210
Africa (SW. Coast)	23°S - 7°S	20°W - 15°E	0.016	0.018	1.35	1.52	0.009	0.012	0.179	0.188
N. America (E. Coast)	30°N - 45°N	80°W - 60° W	-0.008	-0.010	1.07	1.50	-0.015	-0.016	0.157	0.160
Africa (SE. coast)	27° - 15°S	32°E - 45°E	0.017	0.015	2.12	1.93	0.010	0.009	0.129	0.158
Southeast Asia	15°S - 10°N	80°E - 120°E	0.014	0.016	0.80	0.86	0.007	0.010	0.176	0.184
Remote Ocean	40°S - 0°	179°W - 140°W	0.007	0.006	N/A	2.32	0	0	0.100	0.107

834

835

836



844 Table 4. Instantaneous SW aerosol direct forcing efficiencies estimated based on the multi-year means (2000-2015 for Terra and
 845 2002-2015 for Aqua) as well as for Dec.-May and Jun.-Nov. seasons using both CERES SSF and ES-8 datasets. Forcing efficiencies
 846 are calculated for selected regions that have the maximum $2 \times 2^\circ$ (Latitude/Longitude) bin-averaged AOT > 0.3 , as well as for global
 847 oceans. The multi-year mean AOT and SWARE values are estimated using data from all valid bins. Note that values from this table
 848 are estimated under CERES cloud free (less 1% cloud fraction, and 99% CP) skies and thus regional and global AOT values may be
 849 different from the estimates as shown in Table 2.

	Dec.-May (Wm^2/AOT)			Jun.-Nov. (Wm^2/AOT)			Multi-year Mean (Wm^2/AOT)			Multi-year Mean AOT (0.55 μm)			Multi-year Mean SWARE (Wm^2)			
	Terra		Aqua		Terra		Aqua		Terra		Aqua		Terra		Aqua	
	SSF / ES-8	SSF / ES-8	SSF / ES-8	SSF / ES-8	SSF / ES-8	SSF / ES-8	SSF / ES-8	SSF / ES-8	SSF / ES-8	SSF / ES-8	SSF / ES-8	SSF / ES-8	SSF / ES-8	SSF / ES-8	SSF / ES-8	SSF / ES-8
Africa (NW Coast)	-54.1/ -67.0	-52.7/ -63.0	-59.5/ -75.2	-61.1/ -75.9	-54.4 / -65.9	-54.3 / -62.9	0.189 / 0.189	0.189 / 0.189	0.204 / 0.204	0.189 / 0.189	0.204 / 0.204	-10.3 / -12.5	-10.3 / -12.5	-11.1 / -12.8	-11.1 / -12.8	-11.1 / -12.8
Africa (SW Coast)	N/A/ N/A	N/A/ N/A	40.6/ 44.3	43.0/ 45.0	-37.8 / -39.8	-42.5 / -43.7	0.160 / 0.160	0.160 / 0.160	0.158 / 0.158	0.160 / 0.160	0.158 / 0.158	-6.0 / -6.4	-6.0 / -6.4	-6.7 / -6.9	-6.7 / -6.9	-6.7 / -6.9
Coastal China	-88.3/ -83.8	-84.0/ -82.4	-74.7/ -74.5	-70.8/ -74.4	-79.0 / -79.5	-74.3 / -79.7	0.293 / 0.293	0.293 / 0.293	0.356 / 0.356	0.293 / 0.293	0.356 / 0.356	-23.2 / -23.3	-23.2 / -23.3	-26.5 / -28.4	-26.5 / -28.4	-26.5 / -28.4
Arabian Sea	-62.0/ -75.3	-66.0/ -75.0	-60.0/ -76.0	-60.6/ -76.5	-61.6 / -76.0	-65.2 / -77.4	0.215 / 0.215	0.215 / 0.215	0.238 / 0.238	0.215 / 0.215	0.238 / 0.238	-13.3 / -16.4	-13.3 / -16.4	-15.5 / -18.4	-15.5 / -18.4	-15.5 / -18.4
Bay of Bengal	-66.4/ -69.3	-52.8/ -63.3	-68.4/ -74.8	-58.4/ -67.8	-74.8 / -80.0	-52.3 / -63.1	0.261 / 0.261	0.261 / 0.261	0.295 / 0.295	0.261 / 0.261	0.295 / 0.295	-19.5 / -20.9	-19.5 / -20.9	-15.4 / -18.6	-15.4 / -18.6	-15.4 / -18.6
Global Oceans	-58.7/ -57.9	-57.3/ -59.4	-56.5/ -59.4	-53.7/ -57.2	-60.9 / -57.7	-57.5 / -58.2	0.116 / 0.116	0.116 / 0.116	0.116 / 0.116	0.116 / 0.116	0.116 / 0.116	-7.1 / -6.7	-7.1 / -6.7	-6.7 / -6.8	-6.7 / -6.8	-6.7 / -6.8

850

851

852



853 Table 5 List of uncertainty sources (in $\text{Wm}^{-2} \text{decade}^{-1}$) for the estimated cloud-free SW flux trends.

Region / Sensitivity Test	ES-8/SSF Cloud-free flux trends ($\text{Wm}^{-2} \text{decade}^{-1}$)		Standard Deviation ($\text{Wm}^{-2} \text{decade}^{-1}$)	
	Terra ES-8/SSF	Aqua ES-8/SSF	Terra ES-8/SSF	Aqua ES-8/SSF
Global Oceans / No Data Trim R.O. Region Outline Lat: 40°S - 0° Lon: 180°W - 140°W Lat: 40°S - 0° Lon: 170°E - 150°W Lat: 40°S - 0° Lon: 170°W - 130°W Lat: 50°S - 10°S Lon: 180°W - 140°W Lat: 30°S - 10°N Lon: 180°W - 140°W	-1.50/-1.22 -0.92/-0.70 -1.00/-0.79 -0.84/-0.63 -0.89/-0.67 -1.08/-0.81	-0.50/-0.26 -0.50/-0.25 -0.47/-0.23 -0.43/-0.20 -0.43/-0.25 -0.62/-0.29	0.09/0.08	0.08/0.03
Global Ocean / Variation of CF % 0 <0.5 <1 <2 <3 <4 <5	-1.46 -1.49 -1.50 -1.51 -1.54 -1.56 -1.57 -1.22 -1.24 -1.24 -1.25 -1.27 -1.29 -1.30	-0.46 -0.51 -0.52 -0.54 -0.54 -0.55 -0.55 -0.24 -0.28 -0.28 -0.28 -0.27 -0.26 -0.26	0.04/0.03	0.03/0.01
Global Ocean / Variation of CP % 100 >99 >98 >97 >96 >95	-1.44 -1.48 -1.49 -1.49 -1.49 -1.49 -1.49 -1.13 -1.26 -1.30 -1.32 -1.34 -1.34 -1.35	-0.54 -0.55 -0.54 -0.53 -0.52 -0.52 -0.52 -0.29 -0.23 -0.20 -0.17 -0.16 -0.16 -0.15	0.02/0.08	0.01/0.05
Global Ocean / Cirrus Contamination MODIS-CERES-CALIOP MODIS-CERES-CALIOP (cirrus filtered)		-0.59/-0.33 -0.48/-0.26	0.08/0.05	0.08/0.05
ADMs / Wind Speeds Global Full Data Record (ES-8) Global Full Data Record (SSF)	-1.50 -1.22	-0.50 -0.26	0.20/0.20	0.17/0.17
Overall Uncertainty			0.3/0.3 Wm ² / decade	0.2/0.2 Wm ² / decade



855 Table 6. Inter-comparison of AOT (AOT decade^{-1}) and SW flux ($\text{Wm}^{-2} \text{decade}^{-1}$) trends from this study as well as a few previous
 856 studies at both regional and global scales.

Region	Zhang and Reid (2010) Terra MODIS C5 March 2000- Dec. 2009		$\Delta\text{AOT}/\text{Decade}$		$\Delta\text{AOT}/\text{Decade}$		This Study Terra MODIS C6 March 2000 – Dec. 2015		Toth et al., 2016 Aqua CALIOP Cloud-Free June 2006 – Dec. 2014		Alfaro-Contreras et al., 2016 Aqua CALIOP Above-Cloud June 2006 – Dec. 2014	
	w/o correction	w/ correction	w/o correction	w/ correction	w/o correction	w/ correction	w/o correction	w/ correction	w/o correction	w/ correction	w/o correction	w/ correction
Global Ocean	0.010	0.003	0.008	0.002	-1.50/-1.22	-0.58/-0.52	0.002	0.002	0.002	0.005	0.005	0.0007
Africa (NW Coast)	-0.006	-0.013	0.009	0.003	-1.79/-1.29	-0.87/-0.59	0.003	-0.014	-0.014	0.079	0.079	0.01
Bay of Bengal Coastal	0.076	0.069	0.056	0.050	0.79/0.75	1.71/1.45	0.050	0.016	0.016	0.079	0.079	0.01
China	0.069	0.062	0.007	0.001	-2.51/-2.09	-1.59/-1.39	0.001	-0.017	-0.017	0.01	0.01	0.01
Arabian Sea	0.065	0.058	0.057	0.051	0.90/0.94	1.82/1.64	0.051	0.027	0.027	0.055	0.055	0.055
Med. Sea	-0.009	-0.016	-0.014	-0.020	-2.93/-2.46	-2.01/-1.76	-0.020	-0.006	-0.006	-0.010	-0.010	-0.010
Africa (SW Coast)	0.016	0.007	0.025	0.019	-0.85/-0.57	0.07/0.13	0.019	0.009	0.009	0.007	0.007	0.007
N. America (East Coast)	-0.008	-0.015	-0.016	-0.022	-3.57/-2.73	-2.65/-2.03	-0.022	-0.013	-0.013	-0.02	-0.02	-0.02
Remote Ocean	0.007	0	0.006	0	-0.92/-0.70	0/0	0	0/0	0/0	0.005	0.005	0.005



857 **Figure Captions**

858 **Figure 1.** Spatial distribution of trends for (a) over ocean Terra MODIS DT AOT for 2000-2009,
859 (b) over ocean Terra MODIS DT AOT for 2000-2015, (c) over ocean Aqua MODIS DT AOT for
860 2002-2015 and (d) over land and ocean Terra MISR AOT for 2000-2015 for every $1^\circ \times 1^\circ$ bin. (e)
861 Ratios of MODIS C6 to C5 AOT trends for the study period of 2000-2009, and (f) Differences in
862 MODIS C6 to C5 AOT trends for the study period of 2000-2009. Regions with statistically
863 significant trends at a confidence interval of 95% are highlighted with black dots. Figs. 1e and 1f
864 are constructed with the use of grids with AOT trends above or below ± 0.0002 AOT/year.

865

866 **Figure 2.** (a) The global distribution of daytime AOTs constructed using sixteen years (2000-
867 2015) of monthly-averaged over ocean C6 Terra MODIS AOTs at a $1^\circ \times 1^\circ$ resolution. Only those
868 bins with more than one thousand data counts were considered for this analysis. (b) Similar to Fig.
869 2a, but using over ocean C6 Aqua MODIS AOTs for the study period of 2002-2015. (c) Similar to
870 Fig. 2a, but using both over ocean and over land Terra MISR AOT data for the study period of
871 2000-2015. (d) Differences in gridded AOTs between Terra MODIS and Terra MISR. (e) The
872 ratios of gridded AOTs between Terra MODIS and Terra MISR.

873

874 **Figure 3.** (a) Monthly-averaged global AOTs derived using operational MODIS C6 aerosol
875 products for Aqua (red), Terra (blue) and MISR (green). Straight lines are the linear fits for the
876 monthly data. (b) Similar to Fig. 3a, but for the deseasonalized, monthly-averaged AOTs. (c)
877 Similar to Fig. 3b, but for the Remote Ocean region as described in Table 3.

878



879 **Figure 4.** The deseasonalized, monthly and regionally averaged AOTs for eight selected regions
880 utilizing operational MODIS C6 and MISR aerosol products. Straight lines are linear fits to the
881 monthly data.

882

883 **Figure 5.** (a) The spatial distribution of seasonally-averaged AOTs using Terra MODIS DT AOT
884 data from the collocated Terra MODIS-CERES dataset for the study period of 2000-2015, at a
885 spatial resolution of $2 \times 2^\circ$ (Latitude/Longitude). (b) Similar to Figure 5a but using the collocated
886 Aqua MODIS-CERES dataset for the study period of 2002-2015. (c) Seasonally averaged CERES
887 ES-8 cloud-free SW flux constructed using the collocated Terra MODIS-CERES dataset for the
888 study period of 2000-2015. (d) Similar to Figure 5c, but using the collocated Aqua MODIS-
889 CERES dataset for the study period of 2002-2015. (e-f) Similar to Figs 5c and 5d but for the
890 seasonally-averaged CERES SSF cloud-free SW fluxes. (g) Difference between cloud-free SW
891 flux from Figure 5e and 5c. (h) Similar to Fig. 5g, but for Aqua. (i) Collocated Terra MODIS-
892 CERES data counts for every $2^\circ \times 2^\circ$ (Latitude/Longitude) bin. (j) Similar to Fig. 5i, but for Aqua.
893

894 **Figure 6.** (a) Scatter plot of Aqua MODIS AOT versus CERES SSF SW flux (at a $2 \times 2^\circ$
895 resolution) using data as shown in Fig. 5. (b) Similar to Fig. 6a, but for 5 selected regions that
896 have a maximum AOT > 0.3 as indicated from Fig. 5. (c) Similar to Fig. 6a, but for Terra. (d)
897 Similar to Fig. 6b, but for Terra.

898

899 **Figure 7.** Similar to Fig. 6, but for using collocated MODIS and CERES ES-8 cloud-free SW flux
900 data.

901



902

903 **Figure 8.** (a) Time series of seasonally-averaged, deseasonalized cloud-free SW fluxes over
904 global oceans utilizing the collocated MODIS-CERES (SSF/ES-8) datasets for Terra (green) and
905 Aqua (red). (b) Similar to Fig. 8a but using data from the Remote Ocean region. The ES-8 SW
906 fluxes are depicted by solid lines where SSF SW fluxes are depicted by dashed lines.

907

908 **Figure 9.** Time series of all-sky SW flux over the entire globe (land and ocean). The trends are
909 calculated from monthly-globally averaged all-sky SW fluxes derived from the CERES SSF / ES-
910 8 data. SW fluxes from all scenes including cloudy, clean, land and ocean are taken into account
911 when calculating the monthly averages, which are gridded into a similar resolution as the
912 collocated MODIS-CERES dataset ($2 \times 2^\circ$).

913

914 **Figure 10.** The temporal variations of deseasonalized, seasonally- and regionally- averaged
915 CERES SSF / ES-8 cloud-free fluxes (seasonal anomaly) for 8 selected regions, constructed using
916 the collocated Aqua and Terra MODIS-CERES datasets. The blue lines represent the Terra-based
917 analysis while the red lines represent the Aqua-based analysis and the solid lines represent the ES-
918 8 SW fluxes where the SSF SW fluxes are depicted by dashed lines.

919

920 **Figure 11.** The de-seasonalized, seasonally averaged cloud-free fluxes over the Coastal China
921 region derived utilizing the collocated MODIS-CERES (SSF / ES-8) datasets. Straight lines show
922 linear fits for the study periods of 2000-2008 and 2009-2015.

923



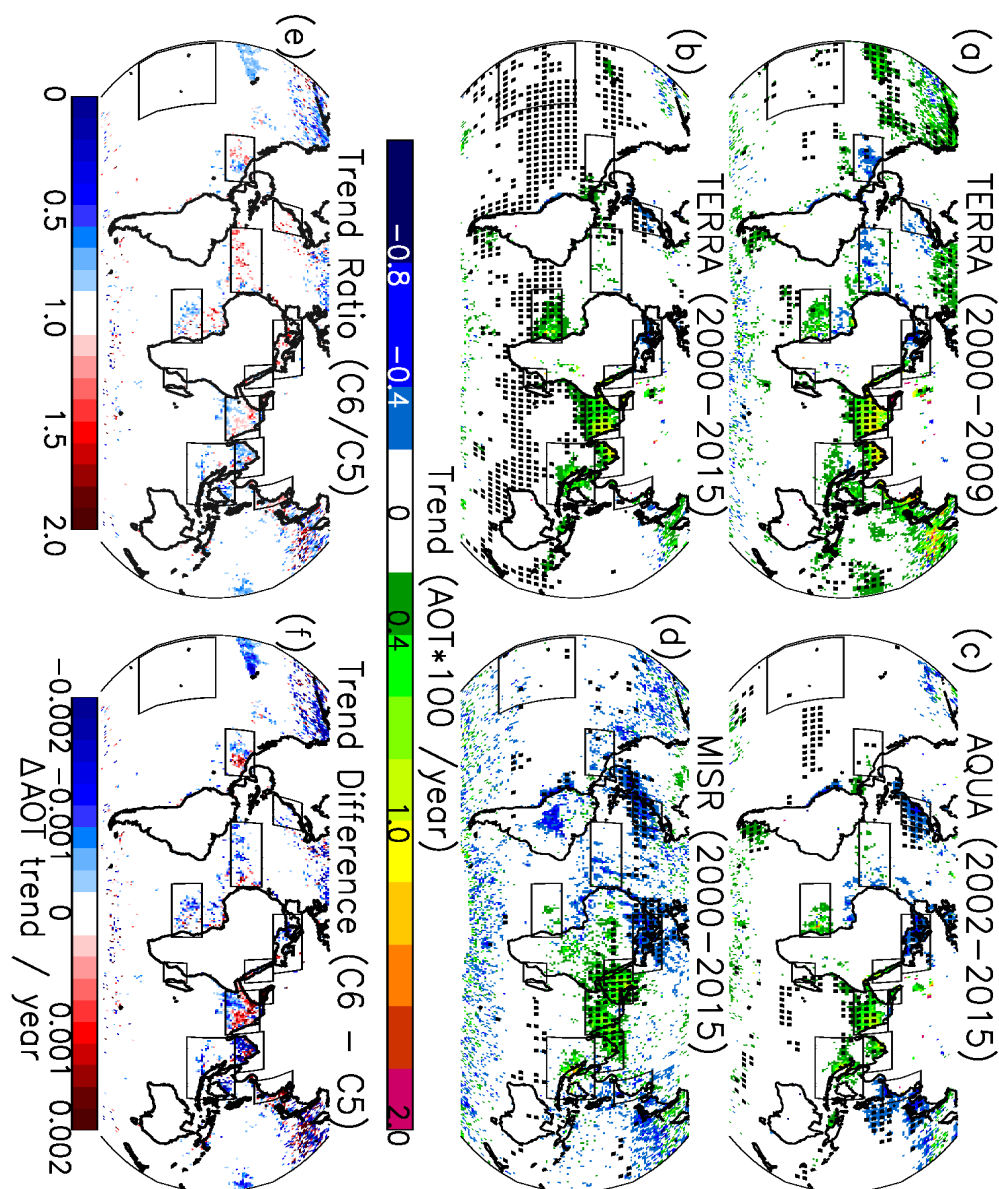
924 **Figure 12.** Spatial distribution of gridded AOT trends for (a) 16 year Terra (2000-2015) and (b)
925 14 year Aqua (2002-2015) for every $4 \times 4^\circ$ (Latitude/Longitude) bin derived from the collocated
926 MODIS-CERES dataset. AOT trends are constructed using seasonally-averaged AOTs. (c) Spatial
927 distribution of cloud-free-sky CERES ES-8 SW flux trends estimated using the collocated Terra
928 MODIS-CERES data for the study period of 2000-2015. (d) Similar to Figure 12c, but using the
929 collocated Aqua MODIS-CERES (ES-8) dataset for the study period of 2002-2015. (e-f) Similar
930 to Figs. 12c and 12d, but for using CERES SSF data. Grids with statistically significant
931 AOT/clear-sky SW flux trends at the 95 % confidence interval are shown in black dots.

932

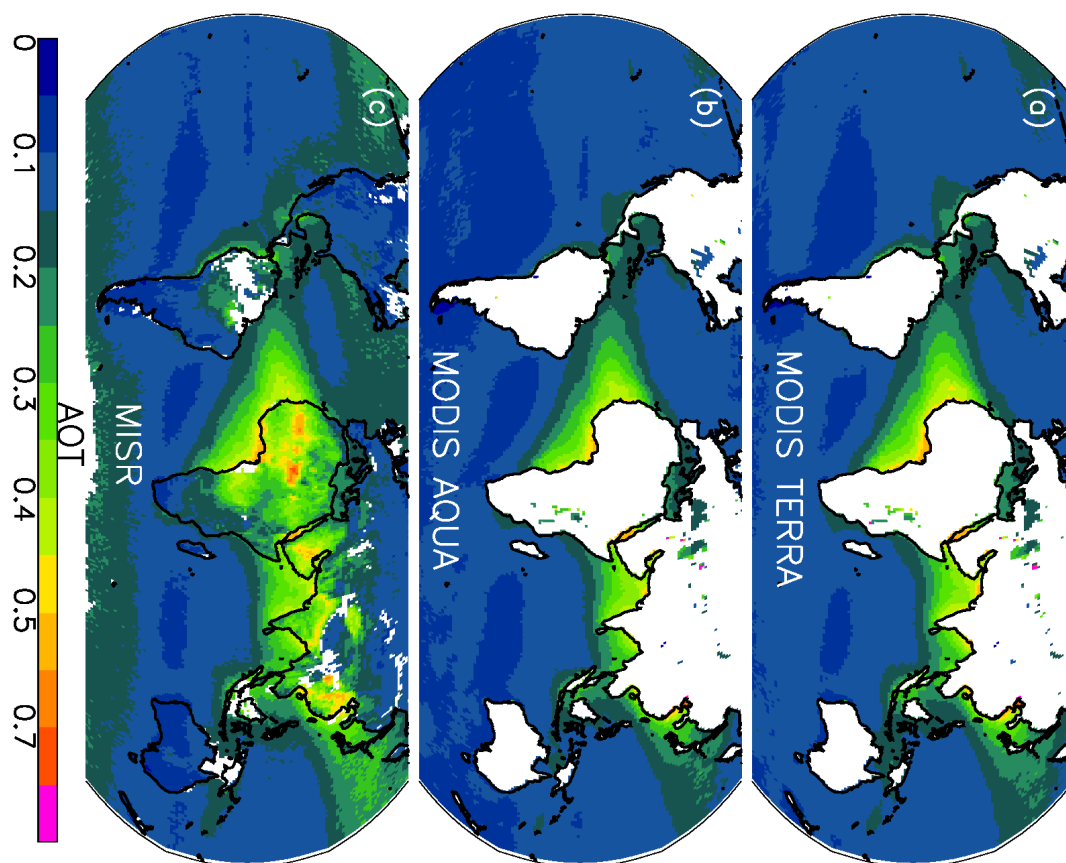
933 **Figure 13.** Global AOT trends derived from the (red) MODIS-CERES dataset, (green) MODIS-
934 CERES-CALIOP dataset and (blue) MODIS-CERES-CALIOP dataset after filtering for cirrus
935 clouds. Both CERES SSF and ES-8 data are included. Time series have been derived utilizing
936 seasonal AOT averages. CALIOP is used to locate and remove CERES observations contaminated
937 with cirrus clouds. (b) Depicts the same thing as Fig. 13a, except for the cloud-free flux. This
938 analysis is carried out for the Aqua-based study only.

939

940



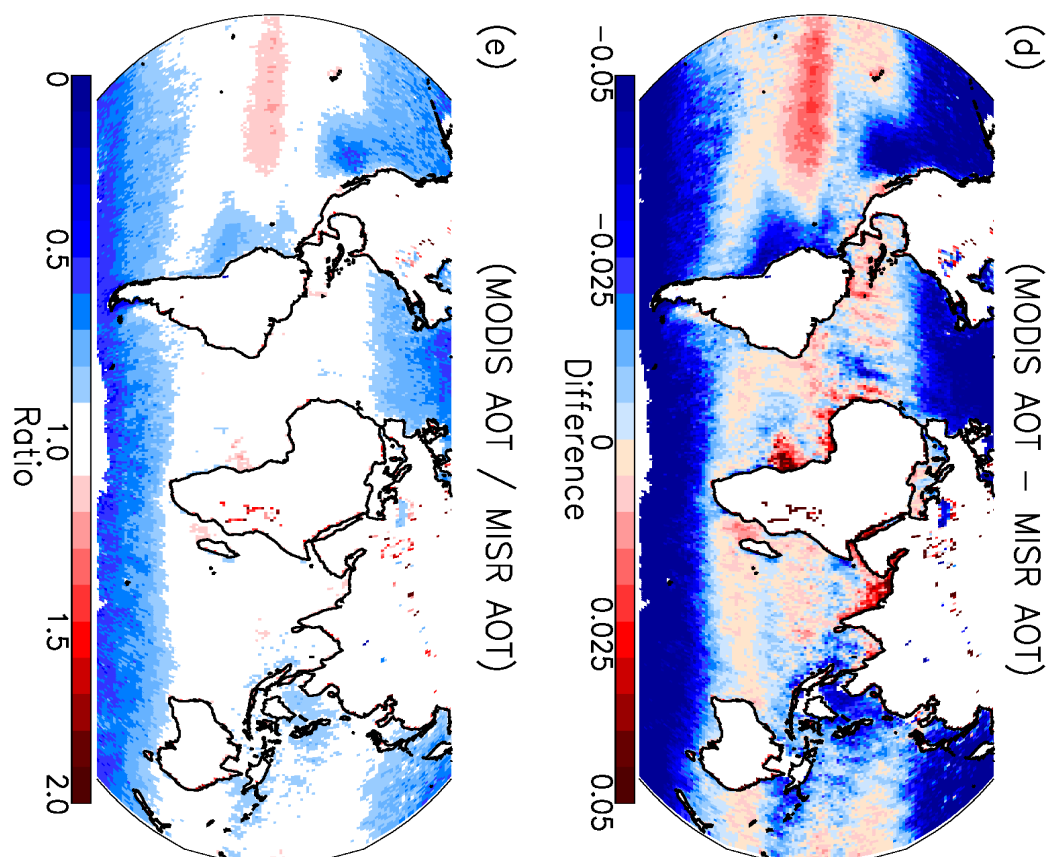
941
 942 **Figure 1.** Spatial distribution of trends for (a) over ocean Terra MODIS DT AOT for 2000-2009,
 943 (b) over ocean Terra MODIS DT AOT for 2000-2015, (c) over ocean Aqua MODIS DT AOT for
 944 2002-2015 and (d) over land and ocean Terra MISR AOT for 2000-2015 for every $1^\circ \times 1^\circ$ bin. (e)
 945 Ratios of MODIS C6 to C5 AOT trends for the study period of 2000-2009, and (f) Differences in
 946 MODIS C6 to C5 AOT trends for the study period of 2000-2009. Regions with statistically
 947 significant trends at a confidence interval of 95% are highlighted with black dots. Figs. 1e and 1f
 948 are constructed with the use of grids with AOT trends above or below ± 0.0002 AOT/year.



949

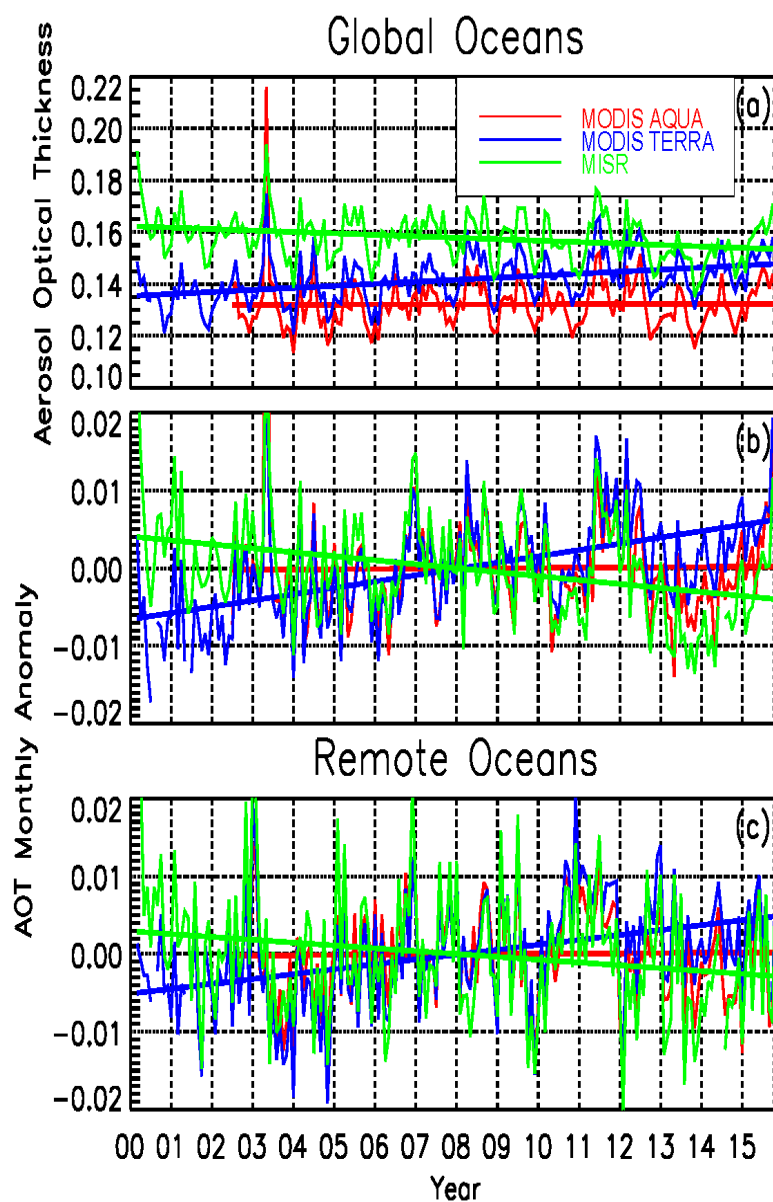
950

951



952

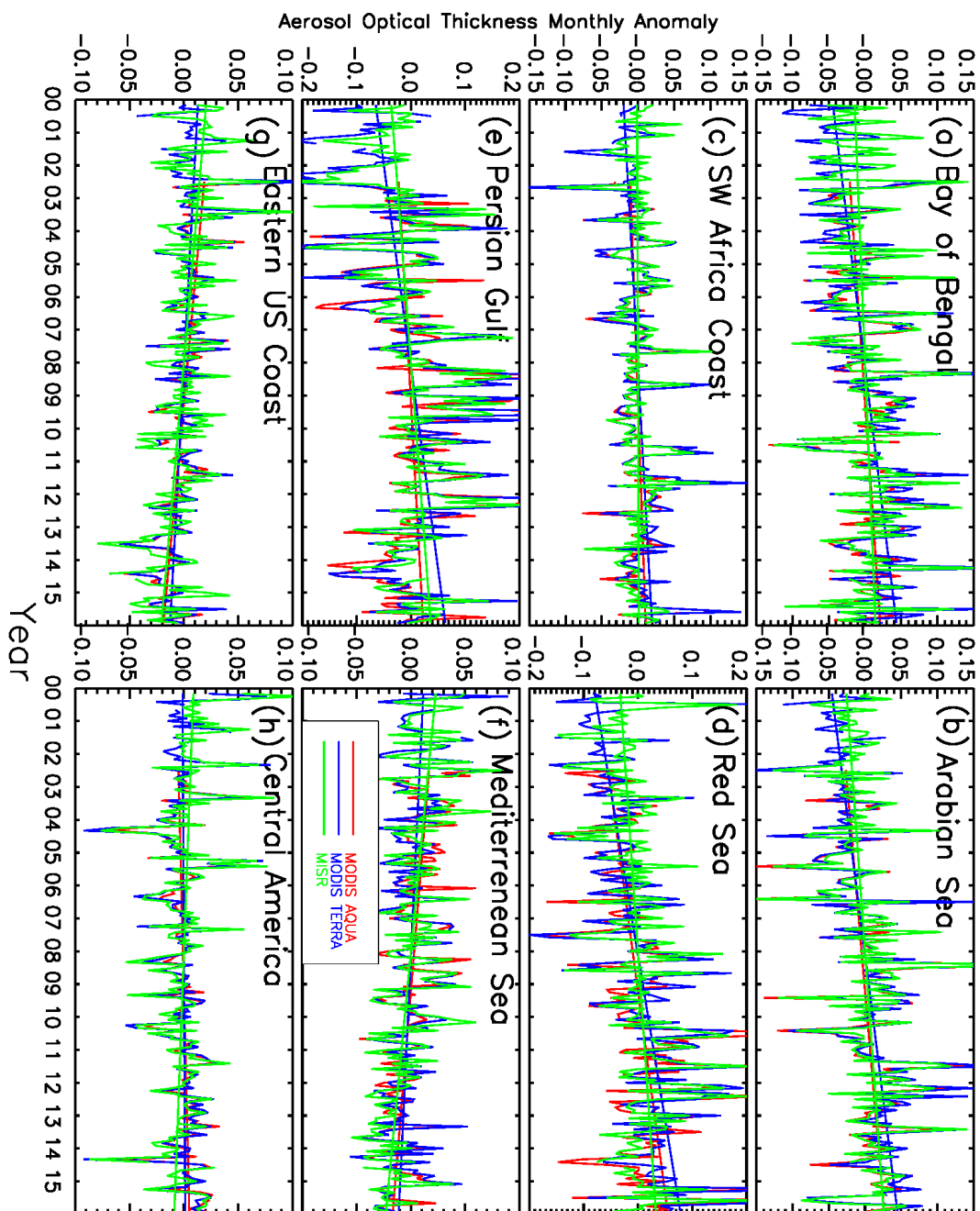
953 **Figure 2.** (a) The global distribution of daytime AOTs constructed using sixteen years (2000-
954 2015) of monthly-averaged over ocean C6 Terra MODIS AOTs at a $1^\circ \times 1^\circ$ resolution. Only those
955 bins with more than one thousand data counts were considered for this analysis. (b) Similar to Fig.
956 2a, but using over ocean C6 Aqua MODIS AOTs for the study period of 2002-2015. (c) Similar to
957 Fig. 2a, but using both over ocean and over land Terra MISR AOT data for the study period of
958 2000-2015. (d) Differences in gridded AOTs between Terra MODIS and Terra MISR. (e) The
959 ratios of gridded AOTs between Terra MODIS and Terra MISR.



960

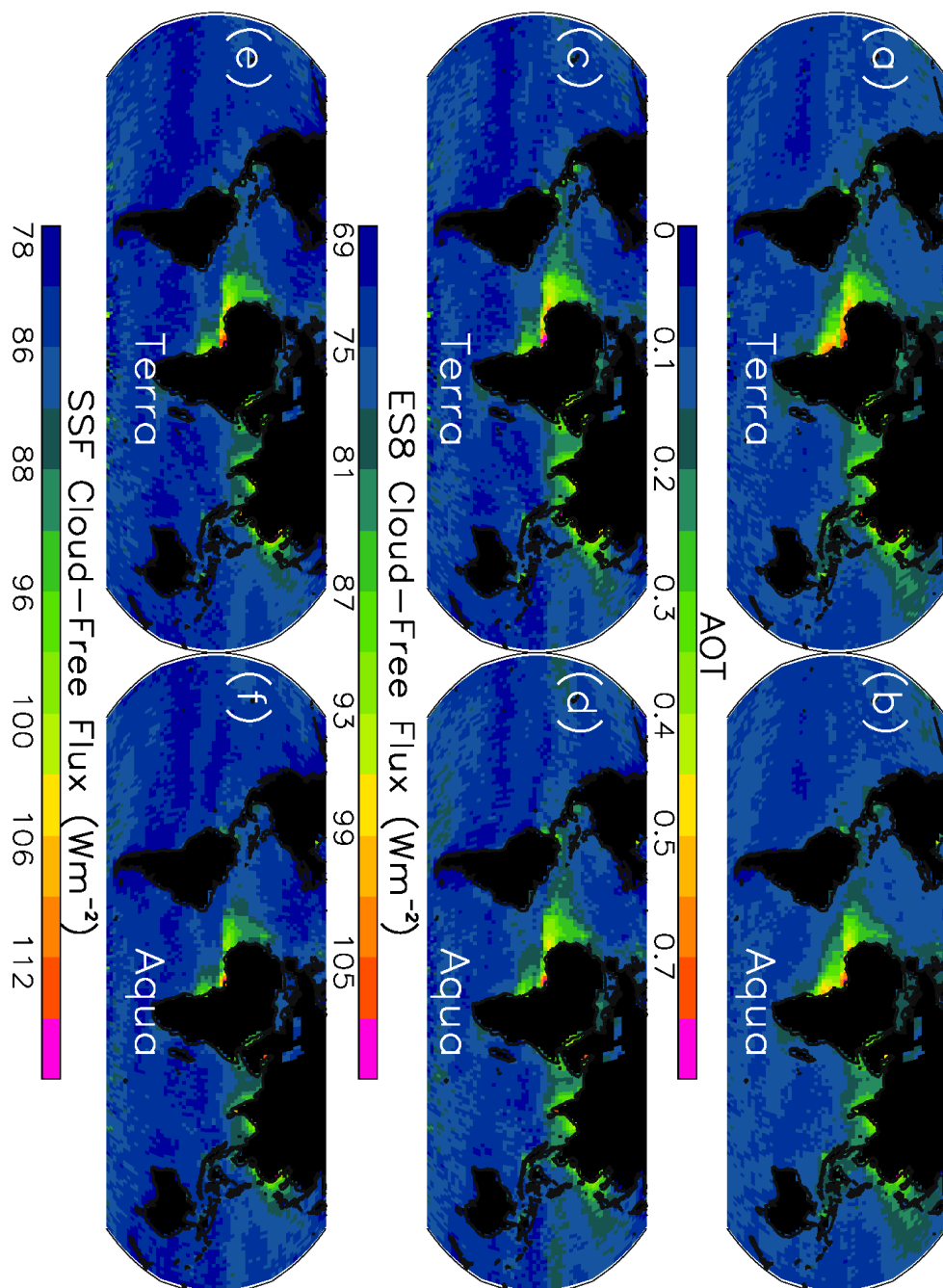
961

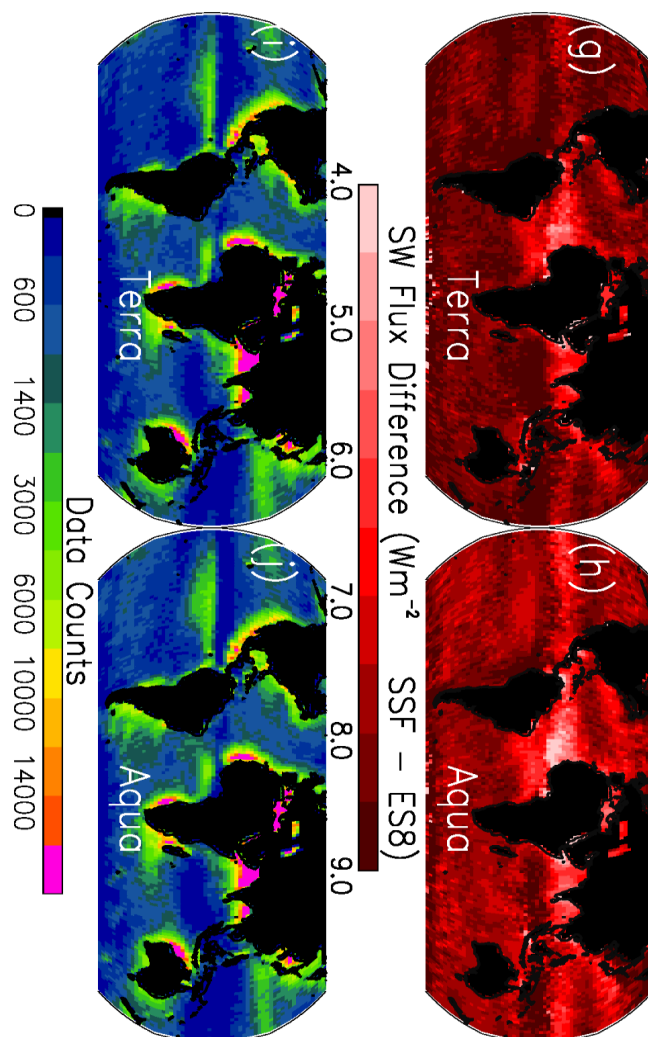
962 **Figure 3.** (a) Monthly-averaged global AOTs derived using operational MODIS C6 aerosol
963 products for Aqua (red), Terra (blue) and MISR (green). Straight lines are the linear fits for the
964 monthly data. (b) Similar to Fig. 3a, but for the deseasonalized, monthly-averaged AOTs. (c)
965 Similar to Fig. 3b, but for the Remote Ocean region as described in Table 3.
966



967

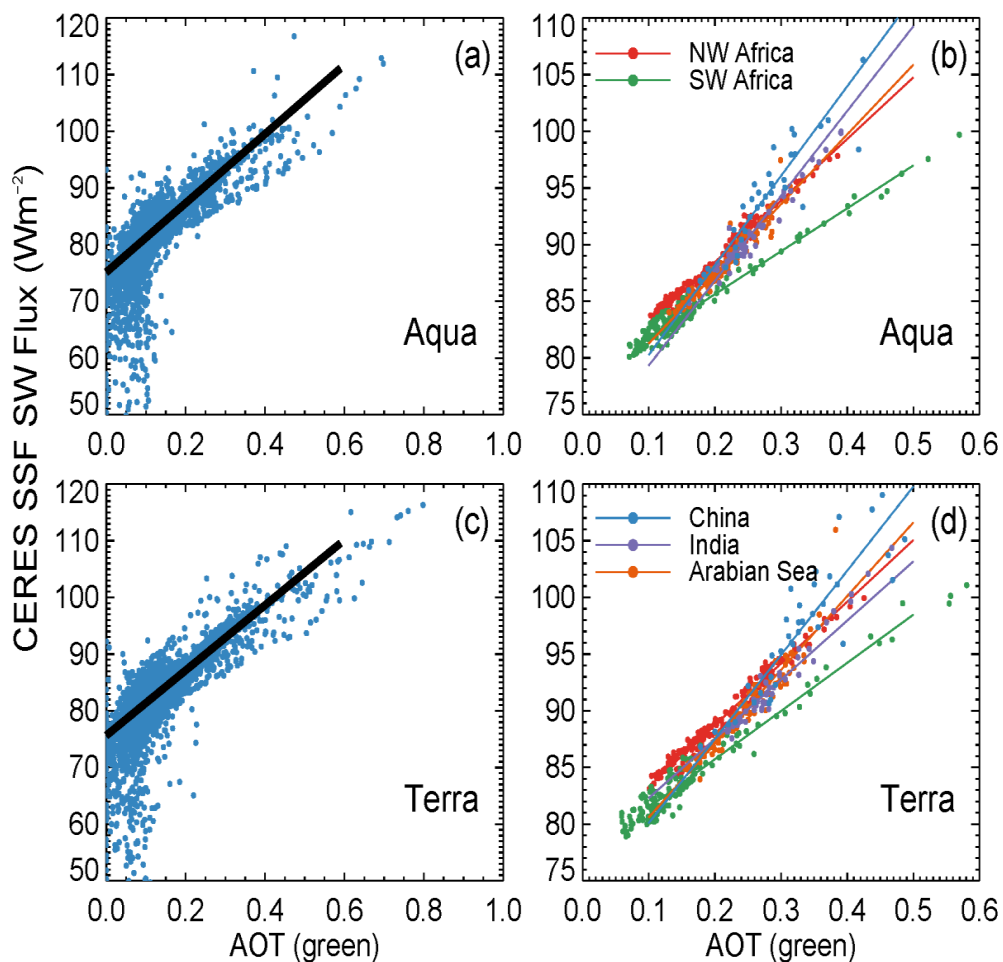
968 **Figure 4.** The deseasonalized, monthly and regionally averaged AOTs for eight selected regions
 969 utilizing operational MODIS C6 and MISR aerosol products. Straight lines are linear fits to the
 970 monthly data.





972

973 **Figure 5.** (a) The spatial distribution of seasonally-averaged AOTs using Terra MODIS DT AOT
 974 data from the collocated Terra MODIS-CERES dataset for the study period of 2000-2015, at a
 975 spatial resolution of $2 \times 2^\circ$ (Latitude/Longitude). (b) Similar to Figure 5a but using the collocated
 976 Aqua MODIS-CERES dataset for the study period of 2002-2015. (c) Seasonally averaged CERES
 977 ES-8 cloud-free SW flux constructed using the collocated Terra MODIS-CERES dataset for the
 978 study period of 2000-2015. (d) Similar to Figure 5c, but using the collocated Aqua MODIS-
 979 CERES dataset for the study period of 2002-2015. (e-f) Similar to Figs 5c and 5d but for the
 980 seasonally-averaged CERES SSF cloud-free SW fluxes. (g) Difference between cloud-free SW
 981 flux from Figure 5e and 5c. (h) Similar to Fig. 5g, but for Aqua. (i) Collocated Terra MODIS-
 982 CERES data counts for every $2^\circ \times 2^\circ$ (Latitude/Longitude) bin. (j) Similar to Fig. 5i, but for Aqua.



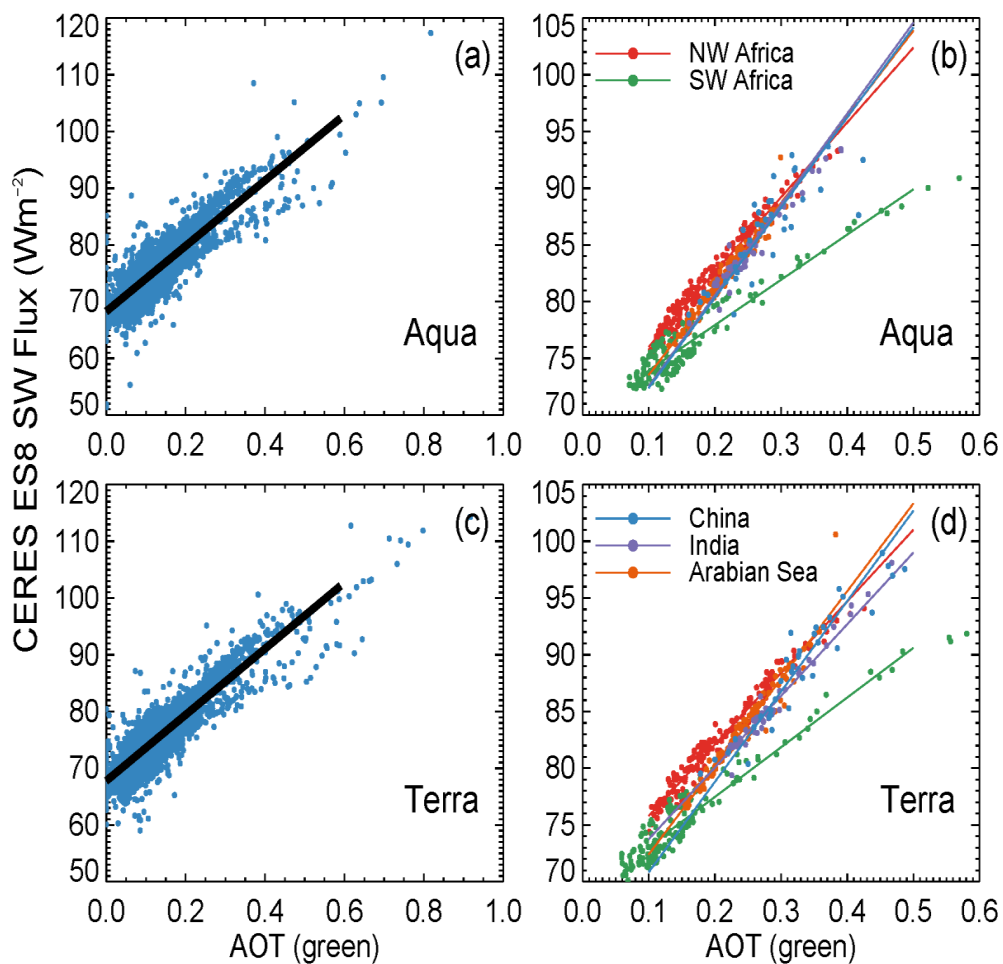
983
984 **Figure 6.** (a) Scatter plot of Aqua MODIS AOT versus CERES SSF SW flux (at a $2 \times 2^\circ$
985 resolution) using data as shown in Fig. 5. (b) Similar to Fig. 6a, but for 5 selected regions that
986 have a maximum AOT > 0.3 as indicated from Fig. 5. (c) Similar to Fig. 6a, but for Terra. (d)
987 Similar to Fig. 6b, but for Terra.

988

989

990

991



992

993 **Figure 7.** Similar to Fig. 6, but for using collocated MODIS and CERES ES-8 cloud-free SW flux
994 data.
995

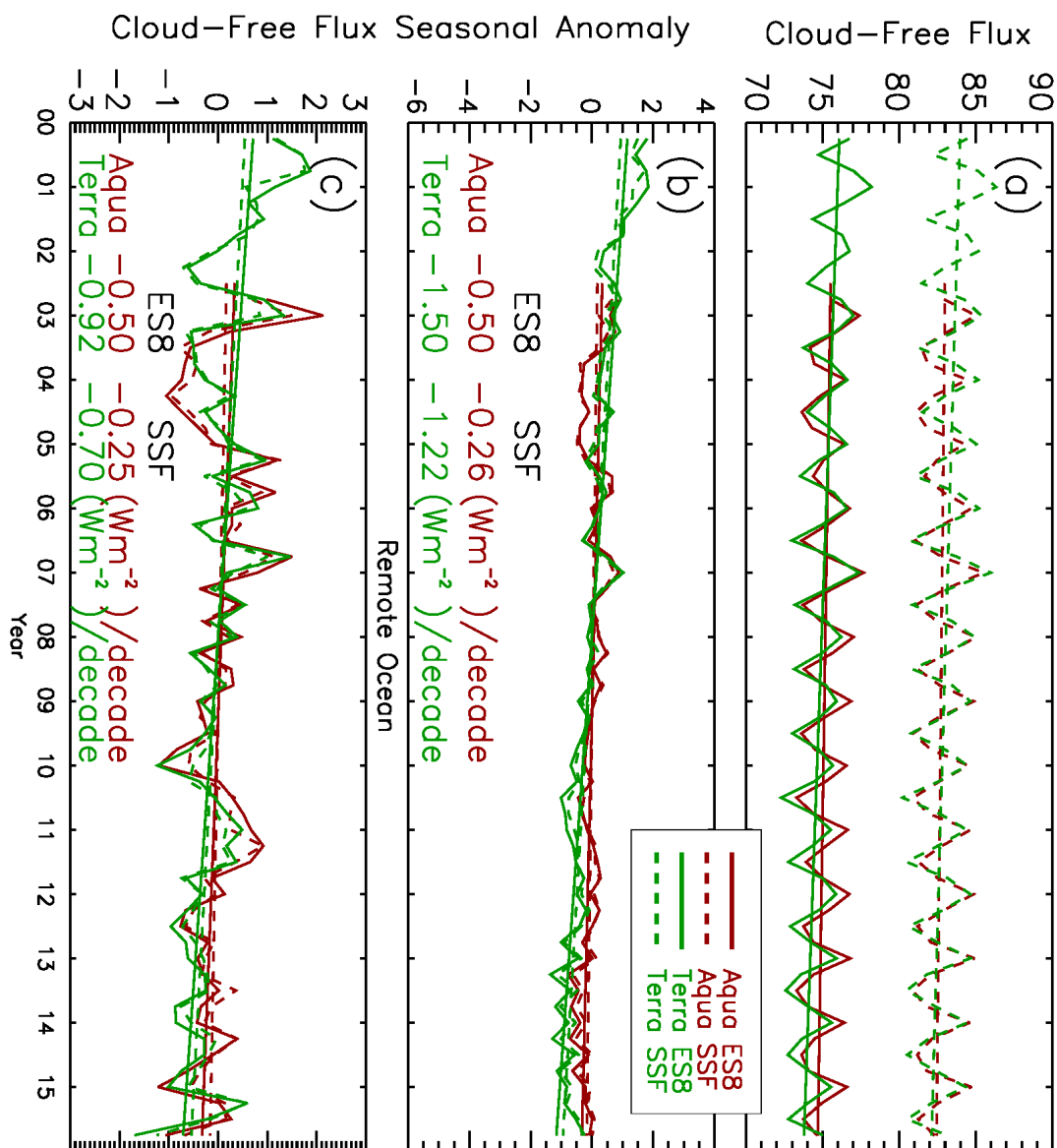
996

997

998

999

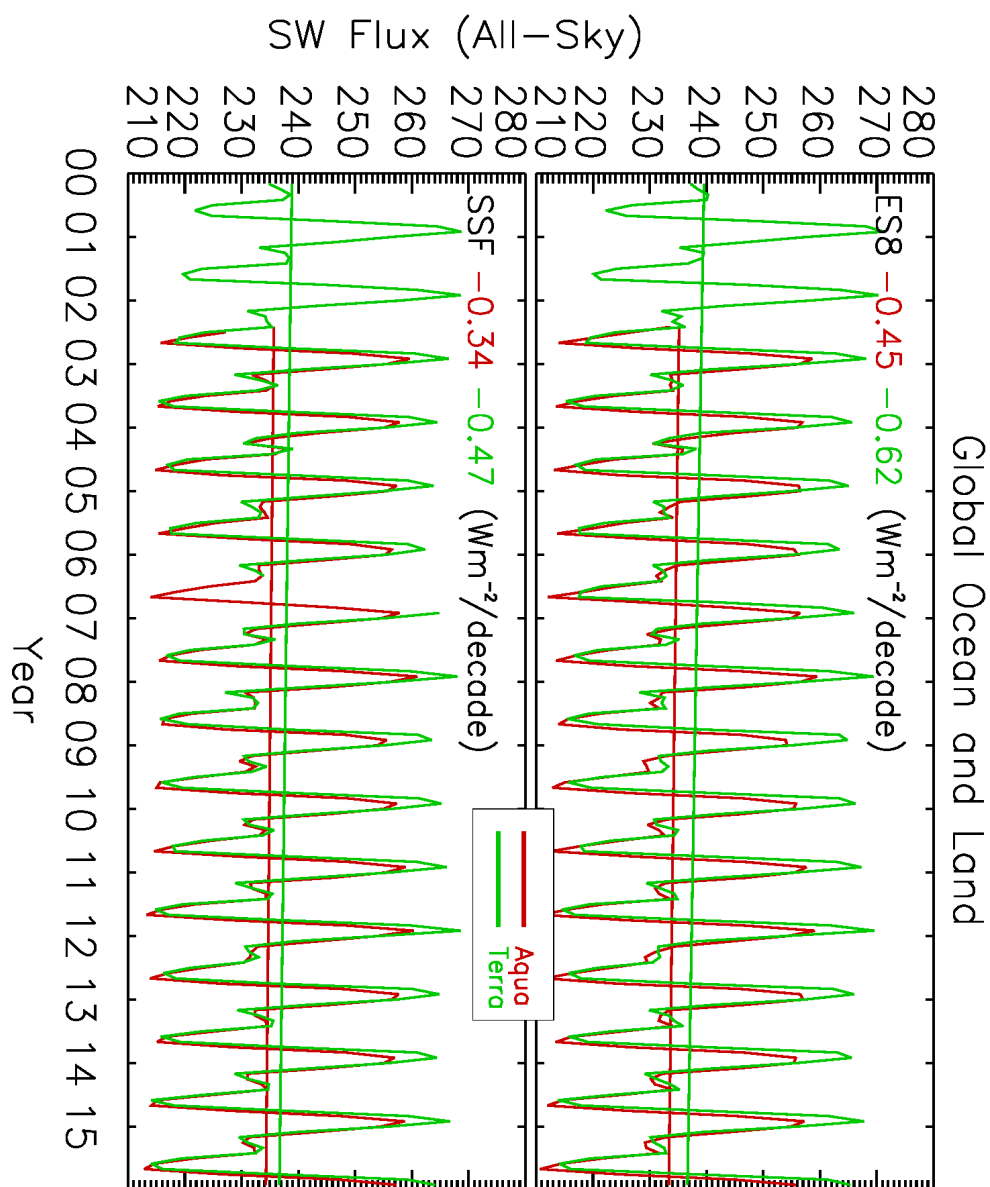
1000



1001

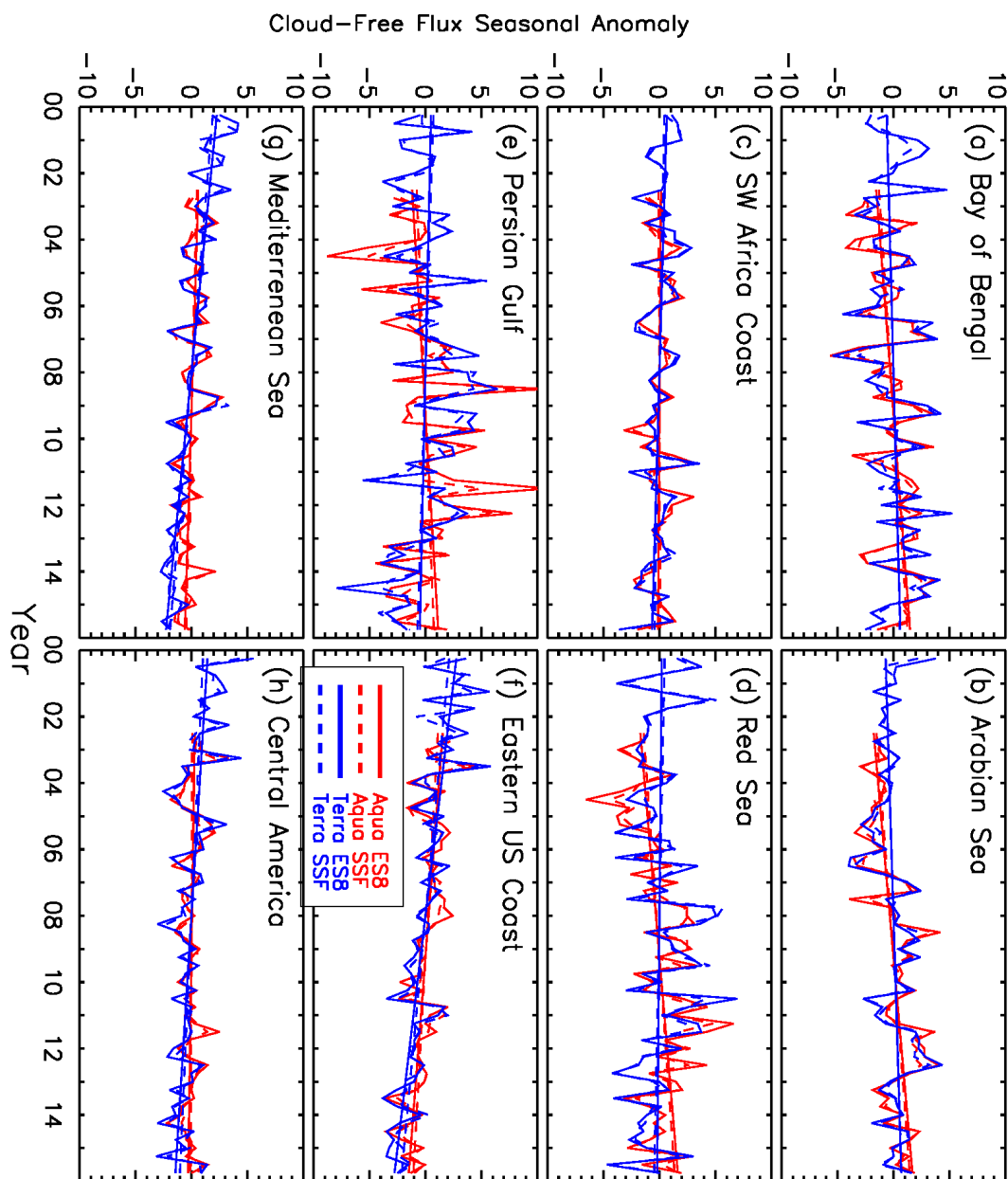
1002 **Figure 8.** (a) Time series of seasonally-averaged, deseasonalized cloud-free SW fluxes over
 1003 global oceans utilizing the collocated MODIS-CERES (SSF/ES-8) datasets for Terra (green) and
 1004 Aqua (red). (b) Similar to Fig. 8a but using data from the Remote Ocean region. The ES-8 SW
 1005 fluxes are depicted by solid lines where SSF SW fluxes are depicted by dashed lines.

1006



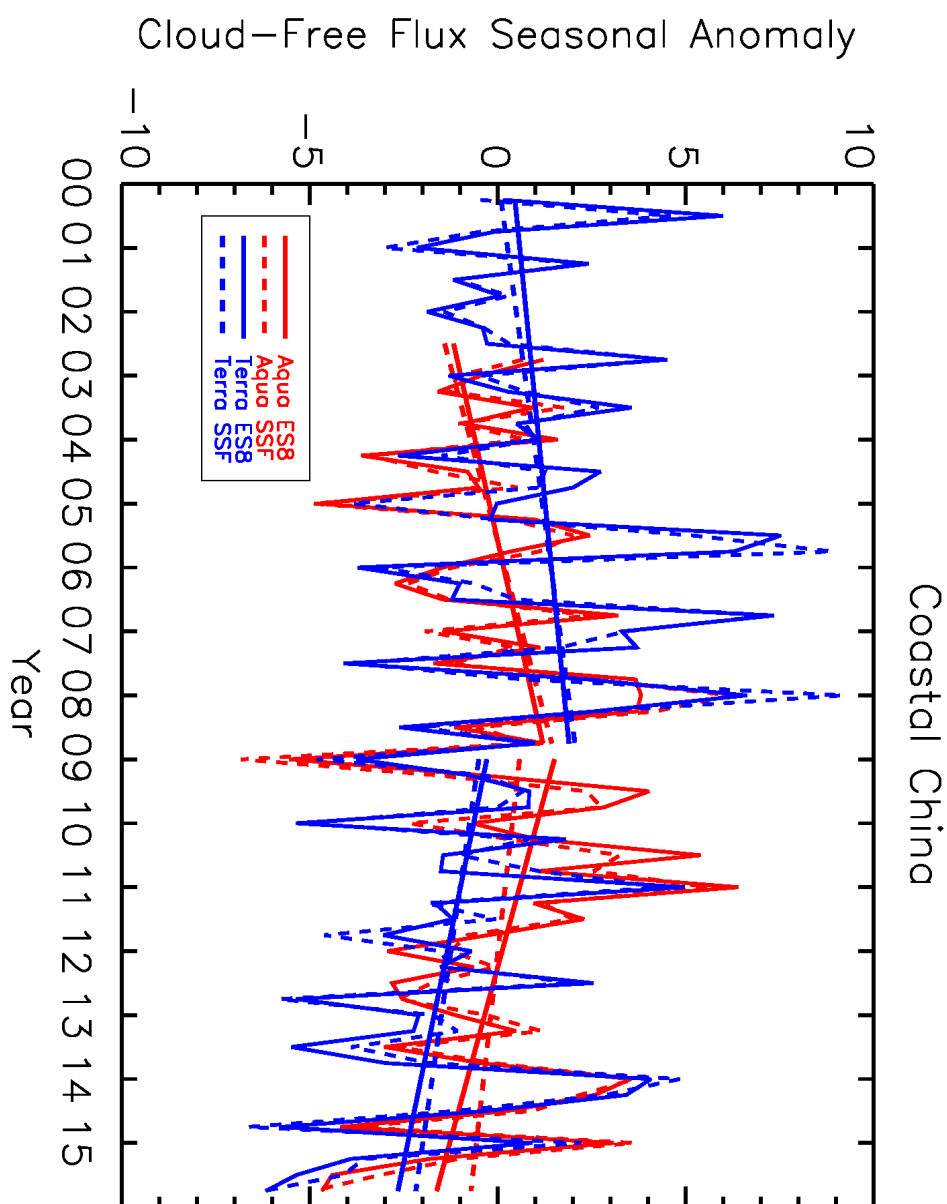
1007

1008 **Figure 9.** Time series of all-sky SW flux over the entire globe (land and ocean). The trends are
1009 calculated from monthly-globally averaged all-sky SW fluxes derived from the CERES SSF / ES-
1010 8 data. SW fluxes from all scenes including cloudy, clean, land and ocean are taken into account
1011 when calculating the monthly averages, which are gridded into a similar resolution as the
1012 collocated MODIS-CERES dataset ($2 \times 2^\circ$).
1013



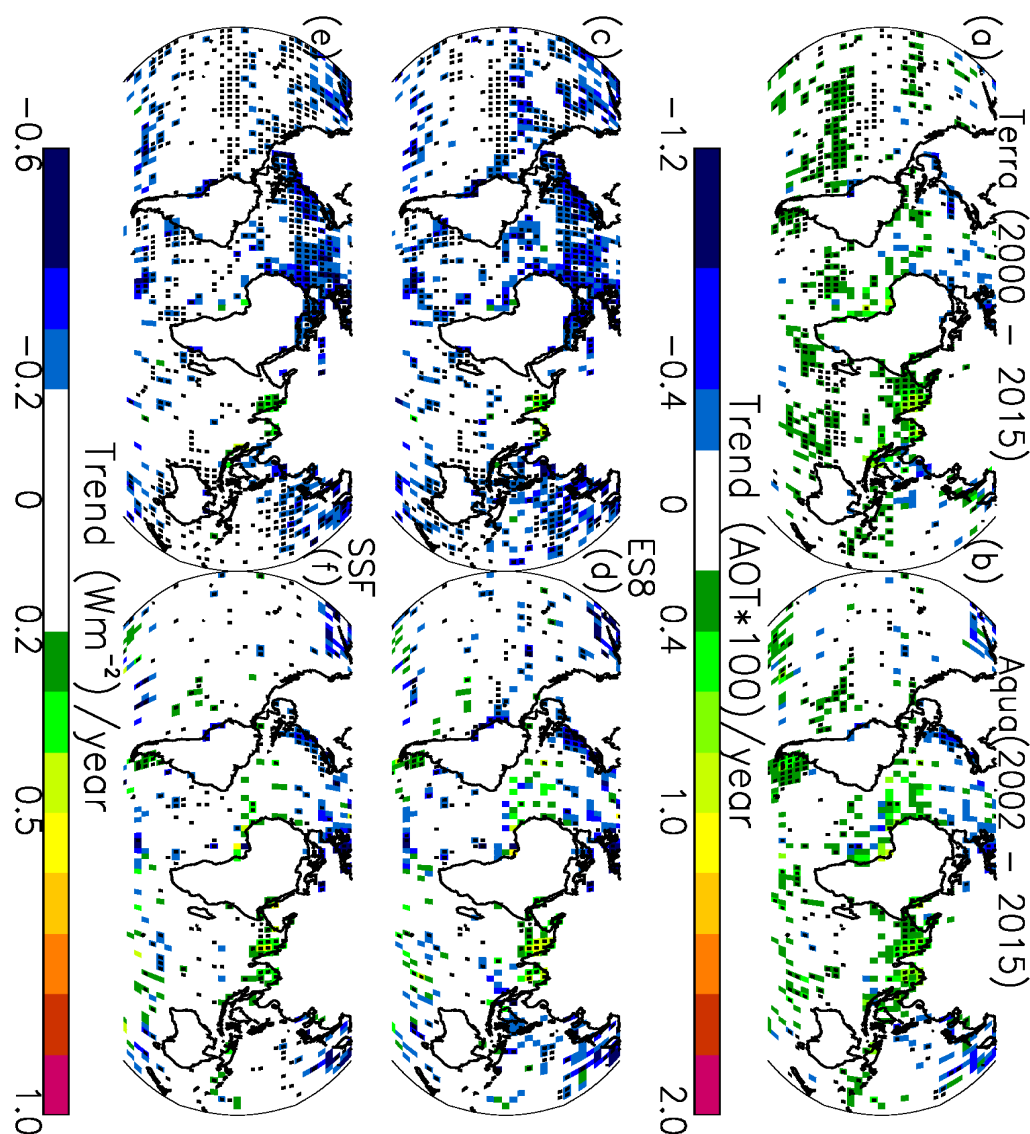
1014

1015 **Figure 10.** The temporal variations of deseasonalized, seasonally- and regionally- averaged
 1016 CERES SSF / ES-8 cloud-free fluxes (seasonal anomaly) for 8 selected regions, constructed using
 1017 the collocated Aqua and Terra MODIS-CERES datasets. The blue lines represent the Terra-based
 1018 analysis while the red lines represent the Aqua-based analysis and the solid lines represent the ES-
 1019 8 SW fluxes where the SSF SW fluxes are depicted by dashed lines.



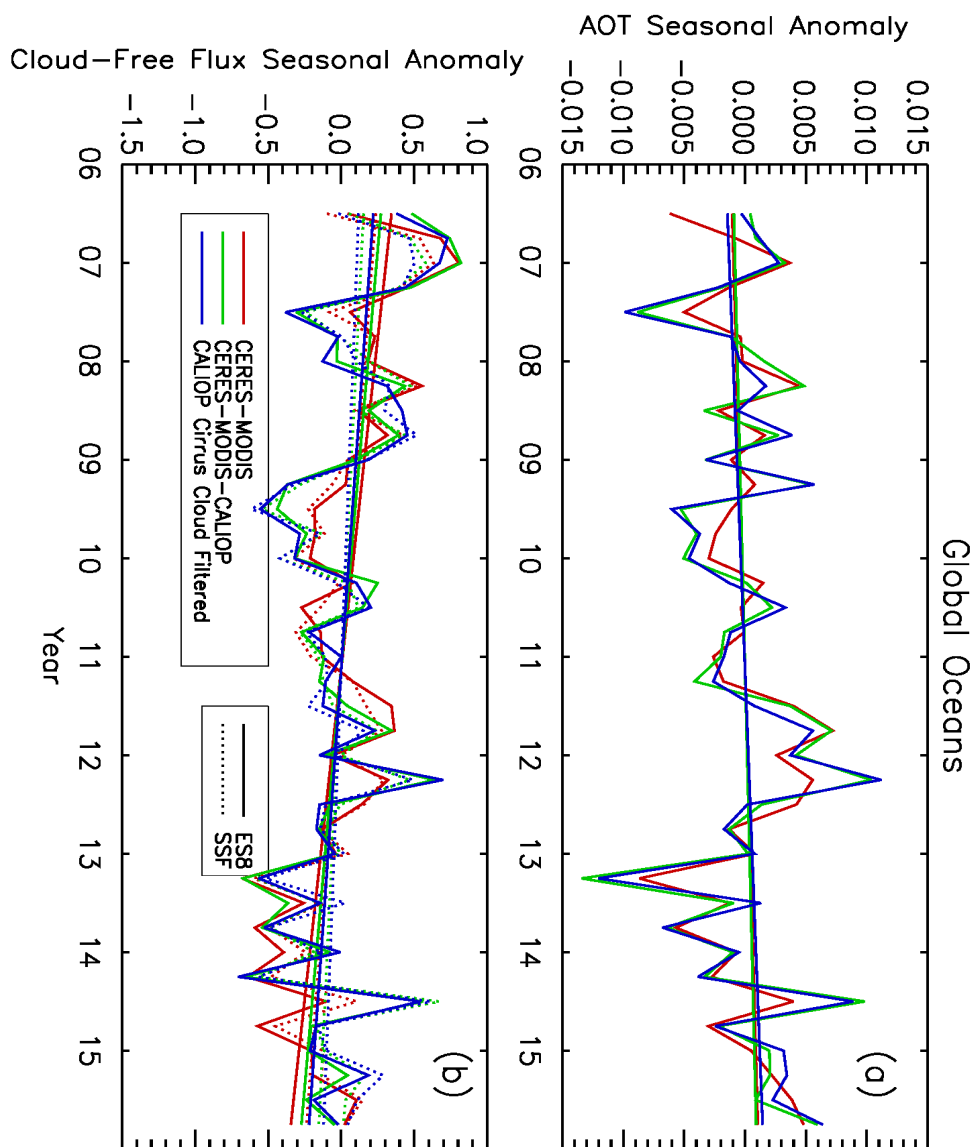
1020

1021 **Figure 11.** The de-seasonalized, seasonally averaged cloud-free fluxes over the Coastal China
1022 region derived utilizing the collocated MODIS-CERES (SSF / ES-8) datasets. Straight lines show
1023 linear fits for the study periods of 2000-2008 and 2009-2015.



1024

1025 **Figure 12.** Spatial distribution of gridded AOT trends for (a) 16 year Terra (2000-2015) and (b)
 1026 14 year Aqua (2002-2015) for every $4 \times 4^\circ$ (Latitude/Longitude) bin derived from the collocated
 1027 MODIS-CERES dataset. AOT trends are constructed using seasonally-averaged AOTs. (c) Spatial
 1028 distribution of cloud-free-sky CERES ES-8 SW flux trends estimated using the collocated Terra
 1029 MODIS-CERES data for the study period of 2000-2015. (d) Similar to Figure 12c, but using the
 1030 collocated Aqua MODIS-CERES (ES-8) dataset for the study period of 2002-2015. (e-f) Similar
 1031 to Figs. 12c and 12d, but for using CERES SSF data. Grids with statistically significant
 1032 AOT/clear-sky SW flux trends at the 95 % confidence interval are shown in black dots.



1033

1034 **Figure 13.** Global AOT trends derived from the (red) MODIS-CERES dataset, (green) MODIS-
 1035 CERES-CALIOP dataset and (blue) MODIS-CERES-CALIOP dataset after filtering for cirrus
 1036 clouds. Both CERES SSF and ES-8 data are included. Time series have been derived utilizing
 1037 seasonal AOT averages. CALIOP is used to locate and remove CERES observations contaminated
 1038 with cirrus clouds. (b) Depicts the same thing as Fig. 13a, except for the cloud-free flux. This
 1039 analysis is carried out for the Aqua-based study only.

1040